AGU PUBLICATIONS

JGR

Journal of Geophysical Research: Planets

RESEARCH ARTICLE
10.1002/2014JE004690

Key Points:
- Sinus Meridiani is compositionally distinct from similarly aged terrains
- Hesperian highland volcanic regions are similar; lower K than older units
- Global homogenization of unconsolidated surface materials has not occurred

Supporting Information:
- Readme
- Figure S1
- Figure S2 and Table S1

Correspondence to:
A. D. Rogers,
Deanne.Rogers@stonybrook.edu

Citation:
Rogers, A. D., and V. E. Hamilton (2015), Compositional provinces of Mars from statistical analyses of TES, GRS, OMEGA and CRISM data, *J. Geophys. Res. Planets*, *120*, 62–91, doi:10.1002/2014JE004690.

Received 9 JUL 2014
Accepted 22 DEC 2014
Accepted article online 29 DEC 2014
Published online 26 JAN 2015

Compositional provinces of Mars from statistical analyses of TES, GRS, OMEGA and CRISM data

A. Deanne Rogers[1] and Victoria E. Hamilton[2]

[1]Department of Geosciences, State University of New York at Stony Brook, Stony Brook, New York, USA, [2]Department of Space Science, Southwest Research Institute, Boulder, Colorado, USA

Abstract We identified 10 distinct classes of mineral assemblage on Mars through statistical analyses of mineral abundances derived from Mars Global Surveyor Thermal Emission Spectrometer (TES) data at a spatial resolution of 8 pixels per degree. Two classes are new regions in Sinus Meridiani and northern Hellas basin. Except for crystalline hematite abundance, Sinus Meridiani exhibits compositional characteristics similar to Meridiani Planum; these two regions may share part of a common history. The northern margin of Hellas basin lacks olivine and high-Ca pyroxene compared to terrains just outside the Hellas outer ring; this may reflect a difference in crustal compositions and/or aqueous alteration. Hesperian highland volcanic terrains are largely mapped into one class. These terrains exhibit low-to-intermediate potassium and thorium concentrations (from Gamma Ray Spectrometer (GRS) data) compared to older highland terrains, indicating differences in the complexity of processes affecting mantle melts between these different-aged terrains. A previously reported, locally observed trend toward decreasing proportions of low-calcium pyroxene relative to total pyroxene with time is also apparent over the larger scales of our study. Spatial trends in olivine and pyroxene abundance are consistent with those observed in near-infrared data sets. Generally, regions that are distinct in TES data also exhibit distinct elemental characteristics in GRS data, suggesting that surficial coatings are not the primary control on TES mineralogical variations, but rather reflect regional differences in igneous and large-scale sedimentary/glacial processes. Distinct compositions measured over large, low-dust regions from multiple data sets indicate that global homogenization of unconsolidated surface materials has not occurred.

1. Introduction

The Martian surface is dominated by primary igneous minerals (feldspar, pyroxene, and olivine) and one or more "high-silica" phases (volcanic glass, secondary silica, zeolites, opal, and/or poorly crystalline silicates), with local-scale outcrops of sulfate-bearing, carbonate-bearing, and/or phyllosilicate-bearing units [e.g., *Bell*, 2008, and references therein]. Global maps of these minerals using a variety of techniques and spatial scales reveal compositional associations with terrain age, geologic setting, and surface properties, which have been used to infer the processes and events that produced those compositions [*Bandfield*, 2002; *Hamilton et al*., 2003; *Poulet et al*., 2007; *Ruff and Christensen*, 2007; *Koeppen and Hamilton*, 2008; *Ody et al*., 2012, 2013]. To date, however, few studies have focused on spatial variations in lithology or mineral assemblage, which is critical for investigating processes that influenced crustal development and alteration. In this work, we apply standard statistical methods to mineral distributions modeled from Mars Global Surveyor (MGS) Thermal Emission Spectrometer (TES) data at a spatial resolution of 8 pixels per degree (ppd). Through multivariate analysis of mineral abundance, we identify new regions that were unrecognized as distinct in previous studies.

Global mineralogic and elemental maps of Mars have been produced using a variety of remote sensing techniques including thermal emission spectroscopy (TIR, ~6–50 μm), visible/near-infrared imaging spectroscopy (VNIR, ~0.3–3.0 μm), gamma ray spectroscopy, and neutron spectroscopy [*Bandfield et al*., 2000a; *Dobrea et al*., 2003; *Rogers and Christensen*, 2007; *Poulet et al*., 2007; *Ody et al*., 2012, 2013; *Boynton et al*., 2007; *Feldman et al*., 2002; *Karunatillake et al*., 2009; *Koeppen and Hamilton*, 2008; *Taylor et al*., 2010; *Gasnault et al*., 2010]. Each technique has different sensitivities and limitations; however, the TIR spectral region is particularly conducive to mapping mineral assemblage. Because electromagnetic energy absorption coefficients for minerals are relatively high in this wavelength range, TIR absorptions from mixture

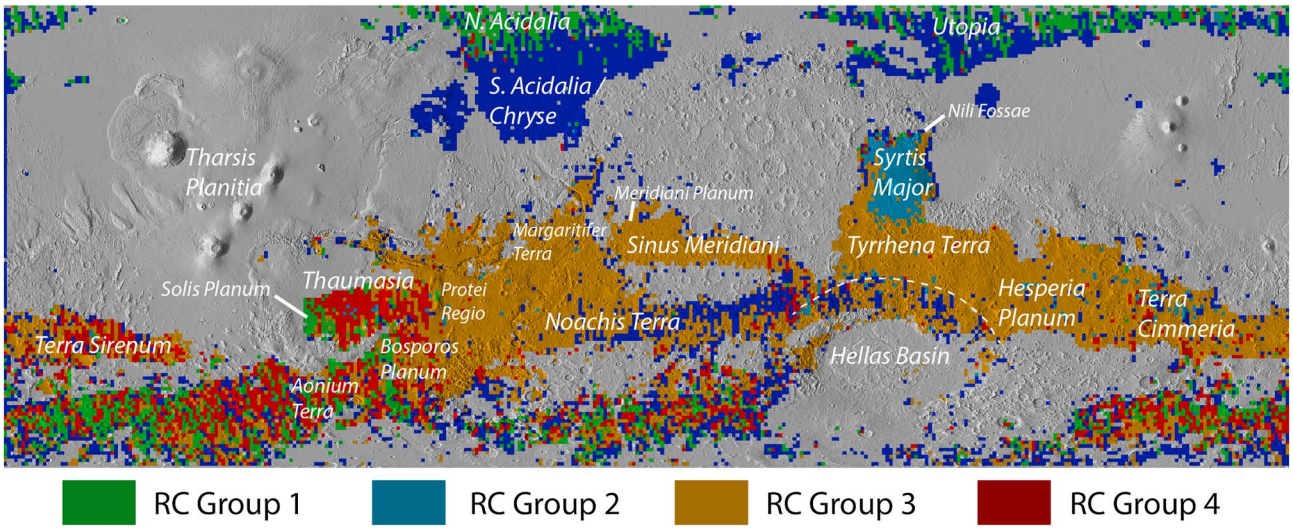

Figure 1. Distribution of compositional classes derived by *Rogers and Christensen* [2007]. The map was generated by color coding each pixel by the dominant compositional class for that pixel. The dark blue class represents low-albedo surfaces that are spectrally distinct from other classes but were excluded from the maps of *Rogers and Christensen* [2007] due to slightly lower spectral contrast and interpreted thin dust coatings. Regions discussed in the text are labeled.

components usually combine linearly for effective grain sizes > ~60 μm, making it possible to quantify mineral abundance over low-dust regions of Mars [e.g., *Ramsey and Christensen*, 1998; *Bandfield*, 2002].

Bandfield et al. [2000a] developed the first compositional class map of Martian low-dust regions using Mars Global Surveyor Thermal Emission Spectrometer (TES) data. The TES instrument provided global TIR coverage of Mars in 143 channels between ~6 and 50 μm. By selecting spectra from multiple low-albedo regions, and then classifying regions based on spectral similarity, *Bandfield et al*. [2000a] discovered two major spectral units on the surface. Surface Type 1 (ST1), found primarily in the Martian highlands, was interpreted as basalt based on spectral similarity to terrestrial flood basalt and on mineral abundance (derived from linear least squares modeling of emission spectra, described in detail in section 2.1). Surface Type 2 (ST2), found primarily in the Martian lowlands and also portions of the southern highlands, was interpreted as basaltic andesite/andesite, again based on spectral comparisons and derived mineral abundance, which includes a significant proportion of amorphous silica rich in Ca and Na (like obsidian or interstitial glass in felsic volcanic rocks). In follow-on TES studies of globally distributed lithologies, *Rogers et al*. [2007] and *Rogers and Christensen* [2007] used an improved spectral library and longer wavelength range to model the spectra of Martian dark regions. They further subdivided Martian surfaces into four subunits (Figure 1). A fifth unit in southern Acidalia was noted as spectrally distinct [*Rogers et al*., 2007] but was interpreted as thin dust cover and was omitted from the maps of *Rogers and Christensen* [2007].

The origin of the silicate glass included in models of Surface Type 2 has been the subject of intense scrutiny. Surface Type 2 has been reinterpreted as an aqueously altered basaltic composition, because some secondary silicates (opals, zeolites, and poorly crystalline silicate phases) are spectrally similar in the TIR to the alkali-rich glass that is used in the best fit models of ST2 [*Wyatt and McSween*, 2002; *Wyatt et al*., 2004; *Michalski et al*., 2006]. GRS data were used to evaluate compositional differences between the northern lowlands (ST2) and southern highlands (ST1). *Karunatillake et al*. [2006] noted that K and Th enrichments were present in the lowlands but that the average K/Th ratios from the highlands and lowlands were not statistically distinct. Together, these observations seemed to suggest that the lowlands represent a geochemically distinct igneous unit, with little evidence to support silica mobilization toward the surface. *Salvatore et al*. [2013] argued that the interpretation of the TIR high-silica component as volcanic glass, amorphous silica, zeolites, or poorly crystalline aluminosilicates is discrepant with near-infrared imaging spectroscopy (NIR) observations. Because most of the high-silica phases exhibit spectral features near ~1.4 and 1.9 μm, due to hydration, these features should be present in NIR observations in the lowlands, yet they are absent. Through detailed TIR and NIR spectral comparison with oxidative weathering rinds on Antarctic basalts [*Salvatore et al*., 2013], they argue that the northern lowlands spectral signatures are most consistent

with oxidative weathering processes in a very dry environment. Despite this compelling case, the fact remains that some amorphous hydrated silica coatings exhibit weak-to-absent hydration features in the NIR region [*Minitti et al*., 2007]. Thus, the role of rinds or other alteration processes cannot be definitively resolved with orbital data alone and the nature of the ST2 signature remains a complex and unresolved problem.

Though the efforts presented by *Bandfield et al*. [2000a], *Rogers et al*. [2007] and *Rogers and Christensen* [2007] were good first steps in identifying global variations in mineralogy, the mapping relied on analysis of a subset of arbitrarily selected low-albedo surfaces on Mars and were also conducted at a resolution of 1 pixel per degree (~60 km/pixel at the equator). Those studies also focused on the dominant surface emissivity shape for each low-albedo region, and thus, variability within the region may have been missed.

In this study, we build on previous work by statistically analyzing and classifying mineral distributions rather than identifying surface types based on spectral shape distributions. We bin our data at a higher spatial resolution (8 ppd) than in prior studies to evaluate smaller-scale variability. We then compare our results to the elemental distributions measured and mapped by the Gamma Ray Spectrometer (GRS) instrument suite, olivine, and pyroxene mineral distributions mapped by the Compact Reconnaissance Imaging Spectrometer for Mars (CRISM) and the Mars Express Observatoire pour la Minéralogie, l'Eau, les Glaces, et l'Activité (OMEGA) instruments, valley network densities mapped by *Hynek et al*. [2010], and crater density-derived surface ages so that we can both validate our results and understand potential relationships between mineralogy, chemical composition, geomorphology, and surface age. We use our results to further contribute to current understanding of the northern lowlands, elucidate new information about igneous processes related to crust formation and evolution, and provide constraints on resurfacing processes and degree of homogenization on a global scale.

2. Data Set Description and Uncertainties

2.1. Data Set Description

The Michelson interferometer subsystem of the TES instrument measured thermal radiance in the ~6–50 μm range. Energy is measured by a 3×2 detector array; each detector has a field of view covering ~3×8 km on the surface for nadir-pointed observations during the MGS mapping mission [*Christensen et al*., 2001]. *Bandfield* [2002] used a linear least squares modeling approach [*Ramsey and Christensen*, 1998; *Smith et al*., 2000] to produce global maps of minerals/phases and mineral classes from TES data, at a resolution of 1 pixel per degree. This method uses a spectral library of potential surface and atmospheric components [*Bandfield et al*., 2000b] plus a blackbody [*Hamilton et al*., 1997] to obtain a linear least squares fit to the measured TES apparent emissivity spectrum. Fit coefficients, once normalized for blackbody and atmospheric concentrations, represent the areal contribution of each component to the spatial footprint of the detector. If the surface components are homogeneously mixed throughout the depth of penetration (tens of microns, e.g., no coatings), the areal fractions represent volume percentages of each mineral. The success of the algorithm is dependent on the spectral library containing an adequate representation of the phases present on the Martian surface, although close matches can yield suitable results at the mineral class level. However, the better the library represents the phases present, the better the model fit will represent the details of Mars' surface mineralogy.

By adding additional spectra of likely Martian phases, *Koeppen and Hamilton* [2008] improved global mineral mapping so that finer variations in compositional detail (solid solution) are discernable relative to those discussed by *Bandfield* [2002]. They generated global mineral maps from TES data using the linear least squares model but using a spectral library (see Table 4 of the study by *Koeppen and Hamilton* [2008], or Table 2 of this work) that differed most significantly from that of *Bandfield* [2002] in that it contained spectra of olivines having intermediate Mg:Fe compositions and by expanding the range of pyroxene compositions to include pigeonite (a low-Ca clinopyroxene) and more Fe-rich orthopyroxene [*Hamilton*, 2000; *Hamilton et al*., 2003]. Most of these added spectra were not available to *Bandfield* [2002] but are common phases in Martian meteorites and thus are likely components of the Martian surface. *Koeppen and Hamilton* [2008] showed that the new spectra were used in best fit models of the global TES data set, leading to a better representation of Martian surface mineralogy. For example, *Koeppen and Hamilton* [2008] found that olivines of intermediate composition are common at abundances of 10–20% throughout the southern highlands,

Table 1. TES-Derived Mineral Abundance Selection Constraints[a]

Criteria	Values
Target temperature (K)	≥ 255
Emission angle	≤ 10
Incidence angle	≤ 80
Orbit range[b]	1 to 6317
Total ice extinction	≤ 0.08
Total dust extinction	≤ 0.15
Image motion compensation	none
Scan length (wave number spacing)	10
Detector mask (spatial coadding)	none
TES albedo[c]	<0.20
Spectral mask (channel down selection or averaging)	none

[a]A description of all database fields are listed at http://tes.asu.edu/documentation/. Additional quality and observational fields from the TES database used in this task: major_phase_inversion 0 0, algor_risk 0 0, spectral_mask 0 0, and detector_mask_problem 0 0.
[b]MGS mapping phase orbit number. To convert to orbit counter keeper number, add 1683.
[c]An initial albedo constraint was used to achieve manageable file sizes. Data were further constrained using the total sum of surface concentrations described in the text.

whereas the maps of *Bandfield* [2002] show virtually no olivine because the available spectra represented compositional end-members (forsterite and fayalite) that are uncommon on Mars.

In this work, we utilize the global mineral concentrations derived from analyses of individual TES spectra by *Koeppen and Hamilton* [2008]. We selected data for our analysis from their database using the quality constraints shown in Table 1, and then we spatially binned the mineral concentrations at a resolution of 8 ppd. Regions above ±60° latitude were excluded due to low surface temperatures that result in inadequate signal-to-noise ratios. Bins associated with low (<50%) total modeled contribution of surface components to each TES spectrum were discarded (atmospheric and blackbody contributions constitute the remaining concentration percentage), to restrict our analyses to surfaces with high spectral contrast. Low-spectral contrast is associated with small particle sizes, which are subject to nonlinear spectral mixing [e.g., *Ramsey and Christensen*, 1998]. This leaves a total of 308,087 bins for analysis out of a possible 2,764,800 bins and results in unavoidable gaps of spatial coverage. Fortunately, over low-dust regions, the gaps are relatively evenly spaced, allowing broad trends in composition to be determined.

We had the choice of using all or a subset of individual mineral distributions. Our choice was guided by considering the typical standard errors on modeled abundances of individual minerals. In other words, if the modeled abundance for a particular mineral is always below the typical standard error associated with that mineral, we can consider the mapped variations to be insignificant. Standard errors on the derived mineral abundances were not computed in the work of *Koeppen and Hamilton* [2008]. To estimate appropriate standard errors for these mineral abundances using minimal computation time, we modeled a low-resolution (1 ppd) version of the TES emissivity data set [*Rogers et al.*, 2007] using the library of *Koeppen and Hamilton* [2008]. Standard errors were calculated for each modeled mineral abundance [*Rogers and Aharonson*, 2008] for each pixel in the 1 ppd data set, producing maps of standard error for each mineral. The error maps were then masked using the sum of the total surface concentrations (>0.50), as described above, and the mean standard error was calculated for each masked mineral distribution (Table 2). Because standard error is not dependent on signal-to-noise or the number of spectra in the average, using a 1 ppd bin size is adequate for these error estimates. This method provides thousands of data points for deriving a representative standard error using the same surfaces and spectral library and is considered to be "typical" standard errors for each mineral and mineral group used in this work. As can be observed in Table 2, the maximum value for each mineral distribution and mineral group is higher than the typical error; however, these maximum values commonly only occur in 1 or 2 pixels out of the full ~300,000 pixels. These may or may not be spurious values; regardless, because they occupy such a small number of pixels, they are not easily visualized on a global map. Thus, in this work, we set a threshold of statistically significant bins to 0.5%. If at least 0.5% of the total bins (~1500 bins) were modeled above the typical standard error, the mineral distribution was included in multivariate analysis. Based on this analysis, we included 34 out of 35 mineral distributions were in subsequent analyses. Only the hedenbergite distribution was excluded (Table 2). Visual

Table 2. Global Statistics[a]

Groups		Estimated Mean Standard Error	Global						
			Average	Standard Deviation	Max	Median	25% (Q1)	75% (Q3)	99.5%
Feldspar		4.1	28.8	6.5	75.0	28.5	24.7	32.5	49.8
Low-Ca pyroxene		5.3	20.1	6.4	67.5	20.8	16.8	24.8	39.9
High-Ca pyroxene		3.3	7.1	5.5	48.0	6.5	2.9	10.6	25.7
Olivine		2.4	5.1	3.6	42.0	4.8	2.3	7.4	16.9
High-silica phases		3.7	19.3	5.9	62.5	18.7	15.6	22.4	39.7
Carbonate		0.7	3.1	1.6	16.2	3.0	2.0	4.0	7.9
Hematite		1.9	2.1	2.2	33.8	1.6	0.2	3.1	10.8
Sulfate		3.3	13.0	4.7	52.4	12.9	10.1	15.8	27.6
Quartz		0.8	0.5	0.6	9.8	0.3	0.0	0.8	3.3
Individual	Group								
1 ol_fo91	olivine	2.6	0.2	0.4	13.2	0.0	0.0	0.1	2.7
2 ol_fo68	olivine	2.4	1.5	1.8	34.5	1.0	0.0	2.4	9.1
3 ol_fo53	olivine	3.1	1.2	1.6	28.7	0.6	0.0	1.8	8.8
4 ol_fo39	olivine	2.6	0.7	1.2	23.6	0.0	0.0	1.1	6.7
5 ol_fo18	olivine	2.4	1.1	1.6	31.2	0.5	0.0	1.7	8.7
6 ol_fo1	olivine	1.8	0.4	0.8	18.3	0.0	0.0	0.5	4.4
7 albite	feldspar	2.6	2.8	2.7	38.6	2.4	0.7	4.0	13.9
8 oligoclase	feldspar	6.6	7.5	6.7	61.5	6.4	2.4	10.8	33.6
9 andesine	feldspar	9.7	4.9	5.9	74.7	3.3	0.0	7.4	30.8
10 labradorite	feldspar	7.5	4.2	4.9	53.2	3.0	0.0	6.4	26.0
11 bytownite	feldspar	7.1	5.5	5.9	66.0	4.3	0.0	8.2	30.3
12 anorthite	feldspar	5.1	4.0	4.3	53.6	2.8	0.5	5.7	22.3
13 diopside	high-Ca pyroxene	6.8	0.7	1.5	39.1	0.0	0.0	0.8	9.1
14 augite_nmnh9780	high-Ca pyroxene	6.0	0.6	1.3	33.6	0.0	0.0	0.6	7.5
15 augite_nmnh122302	high-Ca pyroxene	3.3	5.9	5.3	47.9	5.0	1.4	8.9	24.9
16 hedenbergite[b]	high-Ca pyroxene	3.8	0.1	0.3	18.5	0.0	0.0	0.0	1.8
17 pigeonite	low-Ca pyroxene	5.1	11.5	7.4	67.5	11.0	6.4	15.9	35.0
18 enstatite	low-Ca pyroxene	2.1	2.3	1.9	21.6	2.0	0.8	3.3	9.8
19 bronzite	low-Ca pyroxene	3.6	3.1	3.0	31.2	2.5	0.7	4.5	15.5
20 alh84001	low-Ca pyroxene	7.0	4.0	5.0	59.3	2.6	0.0	6.2	26.1
21 gypsum	sulfate	1.3	5.5	2.9	52.4	5.4	3.7	7.3	14.7
22 kieserite	sulfate	3.3	6.5	4.4	41.8	6.1	3.5	8.8	22.0
23 anhydrite	sulfate	0.8	1.1	1.1	12.5	0.9	0.2	1.6	5.4
24 quartz	quartz	0.8	0.5	0.6	9.8	0.3	0.0	0.8	3.3
25 krichglass	high-silica phase	2.9	3.9	3.5	40.5	3.3	1.2	5.7	17.0
26 silicaglass	high-silica phase	2.9	1.2	1.8	25.4	0.5	0.0	1.7	10.1
27 serpentine	high-silica phase	3.9	0.5	1.2	32.8	0.0	0.0	0.6	7.2
28 illite	high-silica phase	4.3	4.1	4.6	59.4	2.8	0.5	5.8	24.8
29 camont	high-silica phase	5.6	0.4	1.1	31.6	0.0	0.0	0.0	7.0
30 saponite	high-silica phase	3.4	1.9	2.7	44.1	1.0	0.0	2.8	15.2
31 heulandite	high-silica phase	4.8	3.2	3.5	47.9	2.4	0.0	4.8	18.1
32 stilbite	high-silica phase	2.4	4.1	3.2	35.3	3.8	1.8	5.9	15.7
33 calcite	carbonate	0.4	1.3	0.9	8.9	1.2	0.7	1.8	4.0
34 dolomite	carbonate	0.6	1.8	1.2	11.5	1.7	1.0	2.5	5.8
35 hematite	hematite	1.9	2.1	2.2	33.8	1.6	0.2	3.1	10.8

[a]Values were calculated for all pixels that met the selection criteria described in section 2.1. Pixel concentrations were normalized for atmospheric and blackbody concentrations before averaging.
[b]Hedenbergite was excluded from subsequent analyses due to modeled abundance below estimated errors for >99.5% of the pixels. See text for details.

inspection of the 8 ppd hedenbergite distribution shows no evidence of spatially coherent, elevated abundances, further justifying our choice to exclude it.

Figure 2a shows example histograms of the individual mineral distributions, which are important to assessing the statistical distributions (i.e., normal/Gaussian or not) of our data. The distributions have implications for our selection of data analysis methods. Because some mineral abundances are commonly zero (e.g., a surface may have significant fractions of plagioclase, pyroxene, and high-silica phases, but no olivine), nearly all of the mineral maps have two or more histogram peaks, and thus nonnormal distributions. The zeros

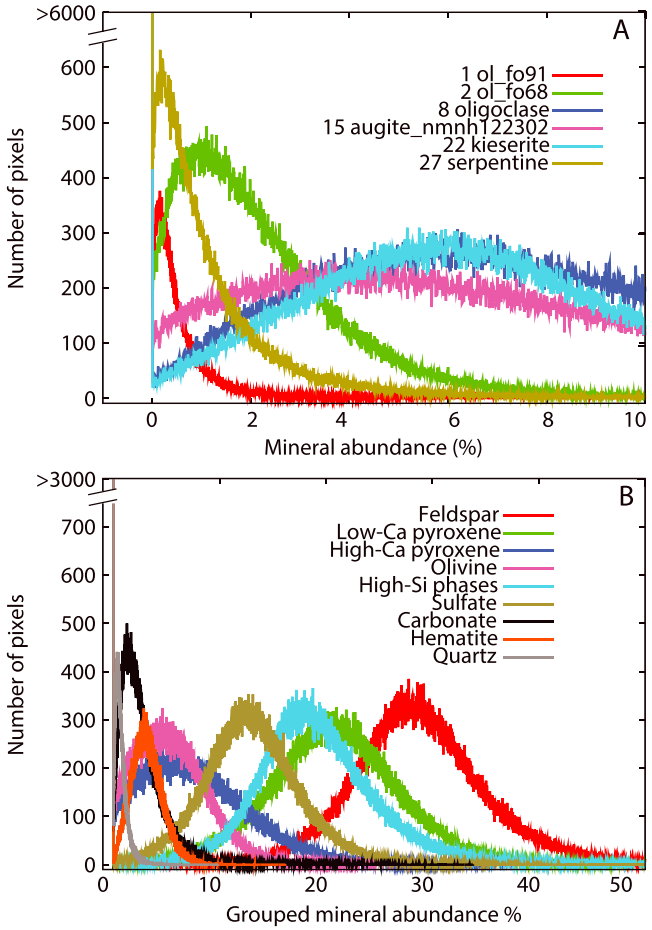

Figure 2. (a) Example mineral abundance histograms for all pixels whose total surface concentrations sum to 50% or greater. Note that nearly all of the histograms exhibit nonnormal distributions. (b) Grouped mineral abundance histograms for all pixels whose total surface concentrations sum to 50% or greater. Each histogram contains 5000 frequency bins and was generated from 308,087 points.

represent meaningful information, as the *absence* of a mineral from a given surface is as important to compositional interpretation as the *presence* of a given mineral. For comparison, Figure 2b shows histograms of grouped mineral distributions, where, for example, individual feldspar (e.g., albite, oligoclase, and andesine) distributions are summed into a single "feldspar" map/group. For the grouped mineral maps, one can see that some mineral groups exhibit normal distributions (e.g., feldspar and low-Ca pyroxene), whereas others do not (e.g., high-Ca pyroxene and olivine). The impact of the non-Gaussian nature of many of the input variables on our analytical approach is described in section 3.2.

2.2. Uncertainties

Though random and systematic errors in TES emissivity spectra are relatively low and minimized by averaging many spectra before modeling [*Christensen et al.*, 2001], there are systematic errors in mineral abundance distributions arising from the atmospheric correction and least squares fitting methods [*Bandfield*, 2002]. These errors can be observed visually in individual mineral distributions, which commonly display between-track "striping" in maps due to variations in atmospheric conditions that may not be properly accounted for in the atmospheric removal step. To overcome these issues and resolve real regional variations present in the data set, a spatial coherence criterion (section 3) was incorporated into our workflow.

There are also mineral abundance uncertainties arising from variations in surface dust contribution. Small amounts of surface dust mixed with coarse-grained sands and rocks may result in systematic use of individual coarse-grained mineral spectra to model the shape of sands plus dust [*Rogers et al.*, 2007]. Correlations between mineral abundance and albedo could arise from this effect. Utilization of only spectra with strong surface signal (total surface concentrations >0.50, as described above) should help to minimize this effect.

Standard errors on individual mineral abundances (e.g., labradorite) are commonly equal to or greater than standard errors for abundances grouped by structural/chemical class (e.g., feldspars) as shown in Table 2. This is particularly the case when there are multiple members of a solid solution series available in the mineral library (e.g., olivines and feldspars) [e.g., *Rogers and Aharonson*, 2008]. This points to the interchangeability of the solid solutions in some (but not all) of the models; for example, an anorthite spectrum may be interchangeable with a slightly less calcic feldspar, depending on what other phases are present in the mixture. Grouped mineral abundances, on the other hand, typically exhibit much lower errors because they account for the covariance of spectrally similar minerals in a group [*Rogers and Aharonson*, 2008]. Despite the higher errors, spatial coherence in an individual mineral distribution, over a given region, may indicate that something about the region is distinct relative to other areas [*Koeppen and Hamilton*, 2008]. But because

the individual mineral errors commonly exceed the modeled abundance, the absolute mineral abundances as well as the presence/absence of specific mineral species can be highly suspect. Thus, in this work, we use the individual mineral distributions for the purposes of identifying similar regions but report only grouped mineral abundances for our final classes.

3. Statistical Methods: Description and Results

The goal of this study was to identify regions of distinct mineral assemblage. Our approach is to start with simple methods for visualization of compositionally distinct regions, to identify spatially coherent regions with the largest differences in mineral abundance values and then to progressively increase the complexity of analyses to identify less extreme differences that still maintain spatial coherence. The spatial coherence criterion helps to place greater significance on distributions with spatial continuity compared to distributions with spatial randomness. This broadly defined approach translates to first identifying regions that exhibit at least one mineral group abundance at the extreme ends of the global population and then using multivariate analysis to identify additional regions of maximum compositional independence from the global data sets. Finally, we present a simplified map that represents these compositional trends by defining regions of interest from these distributions and generating a supervised pixel classification. Below, the description of each statistical method is followed immediately by the results from that method, because the rationale for each subsequent analysis/method is based on results from the previous method.

3.1. Regions With Mineral Groups Modeled With Abundances Greater Than 1 Standard Deviation of the Global Mean

An initial assessment of spatial variability in composition can be determined by examining regions that exhibit mineral group abundances in the upper and lower ranges of the global population. Here we subset the 34 end-member concentration maps by phase structural/chemical characteristics, resulting in nine mineral groups: olivine, feldspar, high-Ca pyroxene, low-Ca pyroxene, sulfate, quartz, high-silica phases, carbonate, and hematite. Figure 2b shows frequency distributions for each major mineral group. Feldspar, low-Ca pyroxene, high-Si phases, and sulfate minerals are generally modeled at nonzero values across the global population, whereas high-Ca pyroxene, olivine, hematite, carbonate, and quartz have truncated distributions indicating that modeled zero abundances are common.

The global average, maximum, standard deviation, and quartile (upper and lower 25%) values for each mineral group are shown in Table 2. Note that the standard deviations are similar to or greater than the typical standard errors, and constitute a high fraction of the mean value ($>$25% in most cases), indicating statistically significant variability across the planet. The lower quartile range includes zero values for some groups; however, none of the lower quartiles are comprised entirely of zero values.

For the six groups that exhibit global mean abundance values above 5%, regions with mineral abundances in the upper and lower ranges of the global population were highlighted by color coding the pixels that were outside of 1 standard deviation from the global mean (Figure 3). Note that because some of the grouped mineral frequency distributions are truncated on one side (e.g., nonnormal, Figure 2), standard deviation values do not necessarily fall on the tail ends of a Gaussian curve, as would be the case for normal distributions. Nonetheless, these "extreme range" maps highlight broad, spatially coherent regions of high and low abundances compared to the global mean. Regions exhibiting the lowest feldspar abundances include Sinus Meridiani (south and east of the Meridiani Planum hematite deposit), as well as areas of elevated olivine abundance, such as Nili Fossae and intercrater plains in Tyrrhena Terra. Lavas in northern and eastern Syrtis Major are enriched in feldspar relative to those in southern and central Syrtis. In the lowland plains, southern Acidalia and Cerberus have lower ($>$4%) than average feldspar (~29%), whereas northern Acidalia exhibits higher ($>$4%) than average feldspar abundance. Pyroxenes are subdivided into low-Ca pyroxene (LCP) and high-Ca pyroxene (HCP). LCP abundances are uniformly low in Syrtis Major and Thaumasia Planum. Portions of Tyrrhena Terra, Hesperia Planum, and Sinus Meridiani also exhibit relatively low abundances of LCP. Regions of elevated LCP are a little more dispersed, with the exception of the highlands within the northern part of the Hellas main basin scarp. High-Ca pyroxene (HCP) is uniformly high in Syrtis Major, Tyrrhena Terra, western Cimmeria Terra, and portions of Margartifer Terra and Thaumasia Planum, and almost uniformly low in the lowlands, southern high latitudes, and northern Hellas rim.

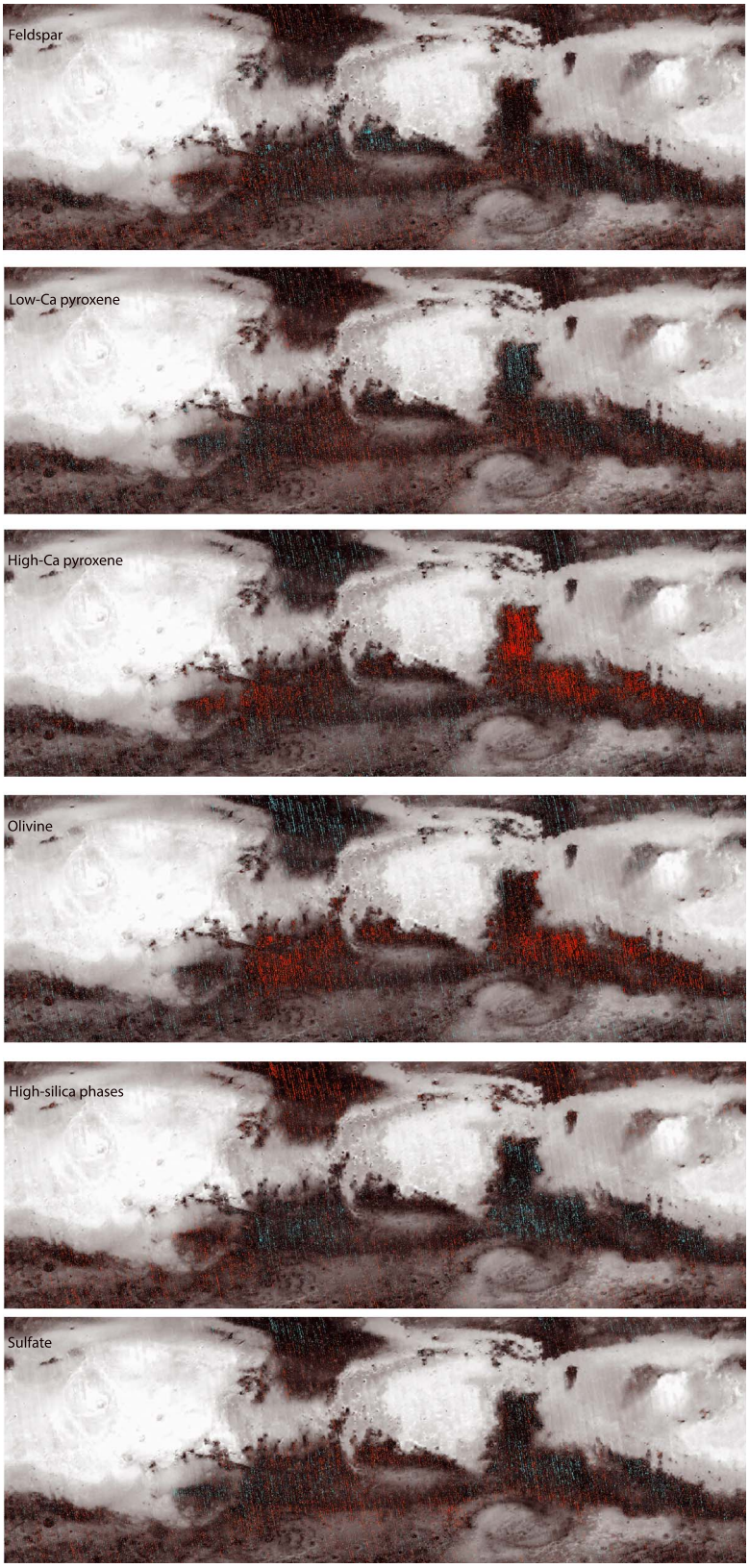

Figure 3. Regions modeled outside of 1 standard deviation from the global mean, for the six major mineral groups. Red pixels contain mineral abundances greater than 1 standard deviation from the mean; cyan pixels contain abundances lower than 1 standard deviation from the mean.

The olivine extreme range map resembles the HCP map (Figure 3), with some notable exceptions. Globally elevated olivine abundances co-occur with globally elevated high-Ca pyroxene abundances in Tyrrhena Terra, Cimmeria Terra, and Margaritifer Terra. However, Syrtis Major and Thaumasia Planum do not show elevated olivine abundances. Olivine abundance is relatively low (as is high-Ca pyroxene) in Acidalia and at southern high latitudes, although some southern high-latitude crater deposits do exhibit elevated olivine abundances [e.g., *Ruff and Christensen*, 2007; *Ody et al*., 2012].

High-silica phase abundance is highest in Acidalia Planitia, Utopia Planitia, and portions of Thaumasia, Aonium Planum, and Bosporos Planum. There are smaller areas of high abundance in regions northwest of Hellas Basin, as well as in west central Syrtis Major. Elevated high-silica abundance corresponding with lava flows in west central Syrtis was noted previously by *Ruff and Christensen* [2007]. High-silica phase abundances are uniformly lowest in western Noachis Terra, Tyrrhena Terra, portions of Cimmeria Terra, and northern Syrtis Major.

Sulfate abundances are highest in southern Acidalia, Sinus Meridiani, and areas near the rim of Hellas basin. Low abundances are observed in northern Acidalia, Tyrrhena Terra, Cimmeria Terra, Thaumasia Planum, and Syrtis Major.

Last, there are regions of Mars that do not appear compellingly distinct in any mineral group, suggesting they are "average." These average areas are located in the southern highlands, generally between ~170 and 280°E, 30 and 55°S. This region hosts Terra Sirenum and volcanic plains south of the Thaumasia rise.

Reducing the information into mineral groups presents a tractable, simple method for identifying broad, regional trends in composition. However, important variations in solid solution could be hidden by the groupings. In addition, this method does not necessarily detect a change in *mineral assemblage*, only a change in a single variable (in this case, a mineral group). To identify changes in mineral assemblage, a multivariate analysis technique is required.

3.2. Multivariate Analysis

To account for the full set of mineral distributions, we used multivariate analysis techniques. Traditional multivariate analysis techniques include image spectral transform and pixel-clustering methods. In this work, we used the independent component analysis (ICA) linear transform technique [*Hyvärinen and Oja*, 2000] to find the most significant variations in the multivariate data as well as to find small-scale regions of interest. ICA has two advantages over principal component analysis (PCA). First, unlike PCA, ICA assumes the independent physical sources have non-Gaussian distributions. As shown above, because some mineral abundances are commonly zero, the distributions for many of the sources are non-Gaussian in nature (Figure 2). Second, because some compositionally distinct regions comprise a small fraction of the pixels used in the analysis, these small but mineralogically distinct regions might only appear in the lower bands of a PCA despite representing a real surface difference.

Individual mineral distributions were first standardized by subtracting the global mean and dividing by the standard deviation. This centers and equally weights the data such that the mean of each mineral distribution is zero and the variance is equal to one. Using the ICA transform function in the commercial software package ENVI 4.8 (ExelisVIS), independent component (IC) bands were then calculated. By using higher-order statistics than PCA, ICA finds directions that maximize independence rather than directions that maximize variance in the data cloud. In this work, directions of maximum independence were estimated using the negentropy optimization method [*Hyvärinen and Oja*, 2000] available in the ENVI 4.8 ICA transform routine.

Because directions that maximize independence do not have variable length, the order of ICA bands are random. This is unlike PCA, where the first PC band contains the most variance in the data, and subsequent bands have decreasing levels of variance. To reduce the dimensionality of the ICA output, a two-dimensional spatial coherence value was calculated for each band, and the bands were then sorted in decreasing order of spatial coherence. The spatial coherence algorithm, available in ENVI 4.8, spatially offsets each IC band by one line and one sample and calculates the correlation coefficient between each original IC band and the spatially offset version of that band. The average of the correlation coefficients for both the line-offset pair and sample-offset pair provide the measure of spatial coherence. This technique is remarkably effective for isolating subtly distinct regions of interest and helps avoid systematic bias in derived mineral abundance caused by imperfect atmospheric separation (observed as spatial correlation with individual orbit tracks).

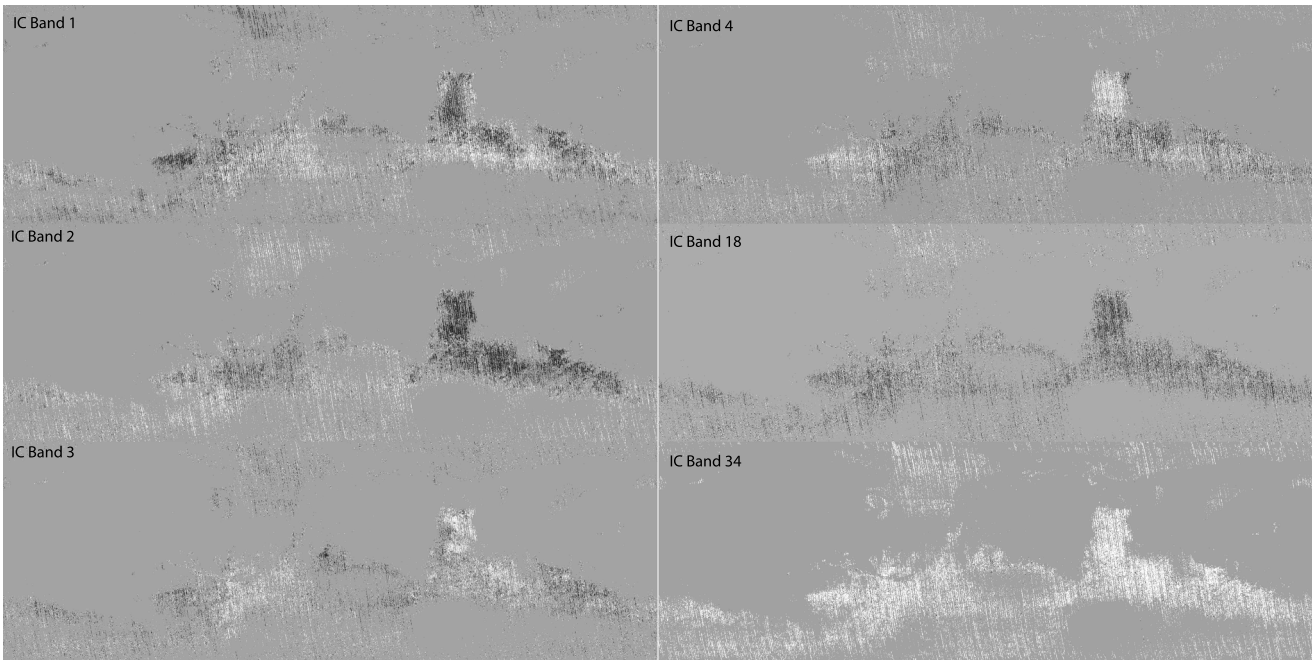

Figure 4. Example results from independent component (IC) analysis and sorting by using the spatial coherence criterion. IC bands 1–4, 18, and 34 are shown. The gray scale indicates the calculated IC factors for each pixel, where black indicates the most negative IC factor and white indicates the most positive factor. The magnitude of the IC factors varies for each image; each image is linearly stretched between the IC factors that comprise the upper and lower 2% (a linear 2% stretch) to show spatial variation. IC bands 1–4 exhibit the highest spatial coherence, and IC band 34 exhibits the lowest spatial coherence. IC band 18 was used as the cutoff for inclusion in the maximum likelihood classification.

Figure 4 shows example bands from the IC analysis. Increasing band numbers indicate decreasing values of the spatial coherence criterion. Example maps with high (bands 1–4), medium (band 18), and low (band 34) spatial coherence are shown for reference. Many of the regions that were highlighted in the grouped mineral analysis are distinct in the IC bands. Below the eighteenth sorted band, little spatial coherence was observed.

Interpretation of IC bands is not straightforward, particularly when there are many input variables. Pearson's correlation coefficients [e.g., *Burt et al*., 2009] between each IC band and each original mineral distribution were calculated to try to understand the relative contributions of each mineral to each IC band. Coefficients of 1.0 or −1.0 indicate a perfect positive or negative correlation, respectively, whereas coefficients near zero indicate a lack of correlation. Table 3 shows that for some of the IC bands showing the most spatial coherence, the highest correlation coefficients (absolute value) range from 0.50 to 0.97 for individual minerals. For mineral groups, correlation coefficients typically stay below ~0.60. In cases where correlation coefficients are generally weak (e.g., less than ~ |0.70|) for all minerals, it is likely that a combination of minerals controls the IC directions with highest spatial coherence, rather than a single mineral. Some indication of *which* minerals control the IC directions can be gained from looking at the strongest positive and negative coefficients for each band. For example, the four highest negative correlation coefficients for IC band 2 are −0.66 (augite), −0.65 (calcite), −0.27 (bronzite), and −0.26 (olivine Fo_{68}), indicating that these four minerals have the most influence, in the negative direction, on the second IC band. These coefficients are low; however, when the augite, calcite, bronzite, and olivine Fo_{68} bands (the four bands with the strongest negative coefficients, suggesting joint control on the second IC band) are combined, the correlation coefficient for the sum of those bands with IC band 2 strengthens to −0.77. This suggests that the right positive and negative combinations of minerals would produce stronger correlations with IC bands. However, there is no easy way to converge on the combination that would produce the strongest correlation coefficient. Thus, the ICA maps are used as a guide for locating regions that are potentially unique, and their boundaries, rather than as compositional indicators.

Journal of Geophysical Research: Planets

10.1002/2014JE004690

Table 3. Pearson's *r* Correlation Coefficients for TES Mineral Abundance Distributions and Top IC Bands[a]

	ICA Band																	
	1	2	3	4	5	6	7	8	9	10	11	12	13	14	15	16	17	18
Mineral Group																		
Feldspar	0.06	−0.09	0.08	0.17	0.27	−0.06	0.01	0.13	−0.25	0.05	−0.32	0.48	−0.01	0.06	−0.12	−0.06	−0.04	0.26
Low-Ca pyroxene	0.15	0.31	0.03	−0.23	−0.33	−0.15	0.14	**−0.55**	−0.04	0.19	0.03	−0.07	0.14	0.21	−0.21	0.02	0.17	−0.07
High-Ca pyroxene	−0.28	**−0.65**	0.04	0.31	0.09	−0.18	−0.03	0.14	−0.05	−0.28	0.17	0.07	0.09	−0.01	0.19	−0.09	−0.02	−0.13
Olivine	−0.10	−0.31	0.03	**−0.55**	0.03	−0.21	−0.06	0.06	0.02	−0.16	0.15	0.00	0.13	0.00	0.04	0.39	0.00	−0.13
High-silica phases	−0.04	0.25	0.04	0.03	0.29	**0.59**	−0.08	0.08	0.37	0.14	−0.02	−0.13	−0.27	−0.30	−0.02	−0.05	0.03	0.16
Sulfate	0.08	0.45	0.02	0.00	**−0.63**	−0.06	0.01	0.29	0.16	−0.05	0.08	−0.25	0.06	0.11	0.00	−0.03	−0.19	−0.19
Hematite	0.02	0.19	**−0.70**	0.12	0.26	0.01	−0.10	−0.06	−0.35	0.06	−0.06	−0.24	−0.13	0.00	0.19	−0.07	−0.02	0.03
Carbonate	0.27	−0.35	0.07	0.21	0.28	−0.02	0.01	0.02	−0.06	−0.04	0.16	−0.37	−0.19	−0.23	0.39	−0.07	0.04	−0.06
Quartz	−0.01	−0.12	0.07	−0.06	0.11	−0.07	−0.02	0.01	0.02	−0.06	0.03	−0.06	0.05	0.00	0.06	0.03	0.00	−0.10
Individual Minerals																		
1 ol_fo91	−0.03	−0.03	0.00	−0.02	0.00	−0.03	0.00	0.01	0.00	−0.01	0.01	0.00	0.01	−0.01	−0.01	0.01	0.01	−0.02
2 ol_fo68	−0.08	−0.26	0.02	**−0.86**	0.00	−0.15	−0.07	0.03	0.07	−0.12	0.10	0.00	0.10	−0.04	−0.03	−0.21	0.00	−0.11
3 ol_fo53	−0.03	−0.13	0.01	−0.13	0.00	−0.11	−0.03	0.01	0.02	−0.08	0.07	0.01	0.07	0.02	0.05	**0.94**	−0.01	−0.07
4 ol_fo39	−0.04	−0.17	0.01	−0.11	0.03	−0.10	−0.03	0.03	−0.04	−0.08	0.08	−0.02	0.05	0.01	0.02	−0.01	0.01	−0.06
5 ol_fo18	−0.03	−0.08	0.03	−0.05	0.04	−0.07	0.01	0.05	−0.02	−0.06	0.08	0.01	0.05	0.03	0.05	0.17	0.00	−0.01
6 ol_fo1	−0.05	−0.11	−0.01	−0.01	0.02	−0.08	−0.02	0.04	0.01	−0.02	0.04	0.00	0.02	0.01	0.01	0.00	0.01	−0.04
7 albite	−0.05	−0.01	0.04	0.03	0.12	−0.11	0.00	0.02	−0.15	−0.09	−0.01	−0.17	0.07	−0.07	−0.43	−0.04	0.00	0.05
8 oligoclase	0.05	−0.01	0.03	0.15	−0.07	−0.03	0.05	0.11	−0.16	0.11	0.02	**0.78**	0.00	0.01	0.03	0.02	−0.08	0.13
9 andesine	0.00	−0.15	0.00	−0.01	0.06	−0.03	−0.05	−0.01	−0.02	−0.05	0.12	−0.08	0.02	−0.02	0.01	−0.01	0.01	0.03
10 labradorite	0.00	−0.18	0.02	−0.09	0.09	0.00	−0.06	0.05	0.05	−0.10	0.07	−0.05	0.01	0.02	−0.05	−0.03	0.02	0.07
11 bytownite	0.01	0.10	0.01	0.03	0.16	−0.02	0.08	−0.05	−0.07	0.04	0.12	−0.07	−0.04	0.06	0.03	0.00	−0.05	−0.06
12 anorthite	0.02	0.15	0.00	0.08	0.03	0.10	−0.04	0.04	0.01	0.08	**−0.92**	−0.11	−0.03	0.04	0.02	−0.05	0.09	0.12
13 diopside	−0.01	0.00	−0.01	−0.04	0.02	−0.02	0.00	−0.01	0.01	0.00	0.00	−0.01	0.01	0.01	0.02	0.01	0.01	−0.03
14 augite_nmnh9780	−0.04	−0.09	0.01	−0.06	0.01	−0.04	−0.02	0.01	0.00	−0.01	0.02	−0.01	0.01	0.02	−0.01	−0.01	0.02	−0.03
15 augite_nmnh122302	−0.28	**−0.66**	0.04	0.35	0.08	−0.17	−0.02	0.14	−0.06	−0.29	0.17	0.08	0.09	−0.02	0.20	−0.09	−0.03	−0.12
16 hedenbergite	0.00	0.00	−0.01	−0.01	0.00	−0.01	0.00	0.00	0.01	−0.01	0.00	−0.01	0.01	−0.01	0.01	0.00	0.00	−0.01
17 pigeonite	0.17	0.37	−0.03	−0.19	−0.43	−0.10	0.06	**−0.57**	0.04	−0.05	0.07	−0.03	0.12	0.19	−0.06	−0.01	0.23	−0.06
18 enstatite	−0.02	0.16	0.07	−0.04	0.21	0.05	0.05	0.02	−0.31	−0.20	−0.03	−0.21	−0.13	−0.10	**−0.67**	−0.01	−0.06	0.00
19 bronzite	−0.19	−0.27	0.04	0.02	0.08	0.08	0.16	0.13	−0.04	**0.83**	−0.15	0.07	0.05	0.07	0.08	−0.04	−0.09	0.09
20 alh84001	0.06	−0.06	0.03	−0.01	0.09	−0.11	−0.02	0.05	0.03	−0.12	0.05	−0.01	0.03	−0.02	0.04	0.07	−0.05	−0.06
21 gypsum	0.05	0.29	0.02	−0.12	−0.27	−0.13	−0.05	−0.45	0.22	−0.11	0.08	−0.07	0.06	−0.19	0.07	0.03	**−0.54**	−0.23
22 kieserite	0.03	0.34	−0.01	0.08	**−0.52**	0.05	−0.16	**0.60**	0.01	0.05	0.02	−0.23	0.09	0.27	−0.05	−0.07	0.09	−0.04
23 anhydrite	0.10	−0.20	0.07	−0.01	0.10	−0.12	**0.83**	0.06	0.05	−0.12	0.06	0.03	−0.28	−0.09	0.03	0.05	0.23	−0.04
24 quartz	−0.01	−0.12	0.07	−0.06	0.11	−0.07	−0.02	0.01	0.02	−0.06	0.03	−0.06	0.05	0.00	0.06	0.03	0.00	−0.10
25 krichglass	−0.04	0.29	0.01	−0.20	−0.21	−0.13	−0.07	0.06	0.02	0.11	−0.09	0.06	0.07	**−0.80**	−0.16	0.03	0.02	−0.15
26 silicaglass	0.02	−0.04	0.00	0.04	0.05	0.09	0.06	0.04	0.00	0.03	0.05	0.00	−0.03	0.07	−0.01	−0.02	0.05	**0.97**
27 serpentine	−0.03	−0.07	−0.02	0.05	0.04	−0.01	0.00	0.00	−0.05	0.01	0.02	0.01	−0.02	0.02	0.00	−0.02	0.02	−0.03
28 illite	0.14	0.08	−0.03	0.08	0.03	**0.96**	−0.03	0.00	0.09	0.01	−0.04	−0.07	0.04	−0.02	0.00	0.02	0.04	0.00
29 camont	−0.02	0.00	−0.01	−0.01	0.02	−0.01	0.00	0.00	0.00	−0.01	0.00	−0.01	0.01	0.01	0.01	0.00	0.01	−0.01
30 saponite	−0.06	−0.11	0.05	0.10	0.13	0.02	−0.01	−0.01	−0.07	0.08	0.03	0.00	**−0.96**	0.00	−0.04	−0.04	0.03	−0.04
31 heulandite	0.03	0.02	0.02	0.00	0.15	−0.10	0.03	0.00	−0.12	0.07	0.04	−0.09	0.10	0.09	0.02	−0.04	−0.03	−0.14
32 stilbite	−0.22	0.15	0.05	0.03	0.39	−0.11	−0.09	0.08	**0.74**	−0.05	0.03	−0.09	0.10	0.22	0.14	−0.05	−0.05	0.10
33 calcite	**0.50**	**−0.65**	0.03	0.19	0.07	−0.07	−0.07	0.02	0.23	−0.13	0.11	−0.05	0.02	−0.15	0.09	−0.11	0.07	−0.04
34 dolomite	−0.01	0.01	0.07	0.14	0.32	0.02	0.06	0.01	−0.24	0.04	0.13	−0.45	−0.27	−0.20	0.44	−0.02	0.00	−0.05
35 hematite	0.02	0.19	**−0.70**	0.12	0.26	0.01	−0.10	−0.06	−0.35	0.06	−0.06	−0.24	−0.13	0.00	0.19	−0.07	−0.02	0.03

[a]Values above ±0.50 are bold, for ease of viewing. The top 18 bands are shown as examples. High *r* values are observed in some of the IC bands between 19 and 34.

3.3. Classification

To produce a single map highlighting major compositional provinces and boundaries, pixels were classified using a maximum likelihood classification [e.g., *Richards and Jia*, 2006, p. 194] on the ICA bands. This classification relies on the input of polygonal regions of interest (ROIs); using results from our analysis of standard deviation maps (Figure 3) and ICA bands (Figure 4), we chose 16 ROIs (Figure 5a). The maximum likelihood supervised classification technique relies on the ROI statistics to calculate the probability that a given pixel in the rest of the data cube belongs in that ROI class. The pixel is then assigned to the class which has the highest probability. In this work, only pixels with greater than 90% probability for a given class were classified.

We performed the classification on the 18 IC bands with the highest spatial coherence values. This allows classification based on spatial meaningfulness rather than random or systematic noise present in the original data set. In addition, reducing the degrees of freedom by nearly half allows for smaller regions of interest to be used in the classification. A recommended minimum number of training pixels within an ROI is 10*N* [*Swain and Davis*, 1978], where *N* is the number of bands. Most ROIs chosen for this study contained $>$180 pixels, ensuring the robustness of the maximum likelihood estimators. The smallest ROI contained 80 pixels (Solis Planum). Note that some regions known to be spectrally unique (e.g., quartzofeldspathic materials in Syrtis Major [*Bandfield*, 2006]), but are areally small (e.g., $<$10 km across), would not be identified through these techniques, as they only constitute ~1–2 pixels out of hundreds of thousands in an 8 ppd data set.

Though maximum likelihood estimators assume normal distributions [*Richards and Jia*, 2006, p. 196], application of the maximum likelihood classification appears to yield reasonable results in this work. Classified pixels are commonly clustered around the original ROI and show spatial coherence (section 4). One reason for this may be that some of the input parameters (the mineral distributions) do have normal distributions within the ROI itself. Finally, we note that the choice of supervised over unsupervised methods was driven by the need to assign higher significance to spatial coherence than to unspatially correlated clusters in the data set. For this particular data set, which clearly contains "striping" due to systematic modeling of certain minerals under varying atmospheric conditions [*Bandfield*, 2002] (section 2.2), unsupervised classification methods failed to identify many of the spatially coherent pixel clusters that were observed in the ICA bands. Thus, we preferred an ROI-based classification method.

Figure 5b shows the resulting class map, which has 16 classes. As a result of the high probability threshold used ($>$90%), only ~17% of pixels were classified. The high number of unclassified pixels points to the uncertainties associated with individual pixels, and the fact that derived mineral abundances vary somewhat from orbit to orbit due to imperfect surface-atmosphere separation (section 2.2). Nevertheless, broad spatial trends in composition can be distinguished.

After the initial classification, we found that some of the class means were indistinguishable from each other, suggesting that some classes should be merged. To determine which classes should be merged, we calculated the spectral "angles" [e.g., *Kruse et al*., 1993] between the class mean abundances of the mineral groups. This method treats each nine-point grouped abundance "spectrum" (the class mean) as a vector and calculates the angle between vectors. Pairs of classes with small angles between them are similar. Class pairs with the smallest angles were iteratively merged until all classes exhibited at least a 10% total difference in absolute mineral abundance. The resulting merged class map is shown in Figure 5c, and final class means and standard deviations are shown in Table 4. Given the uncertainties for individual mineral abundances (section 2.2), class statistics for individual minerals are not reported. Rather, class means and standard deviations are given for each mineral group (Table 4). In addition, class characteristics are reported in the original mineral group abundance space, rather than standardized or IC space, for ease of interpretation. A spatially degraded version of Figure 5c is shown in Figure 5d.

Boundaries observed by *Rogers and Christensen* [2007] and *Rogers et al*. [2007] are preserved in the information class map given in Figures 5c and 5d. Notable class boundaries from those previous works were (1) the southern boundary of Syrtis Major, (2) the boundary between Thaumasia Planum and cratered highlands to the west, and (3) the boundary between northern and southern Acidalia. The class map in Figure 5 shows not only those boundaries but also a few more potential divisions within the original regions defined by *Rogers and Christensen* [2007]. For ease of presentation and discussion, the potential new compositional divisions are compared with the original classification of *Rogers and Christensen* [2007], which included four groups (Figure 1). These are hereafter referred to as "RC Group #." Finally, in some cases, the

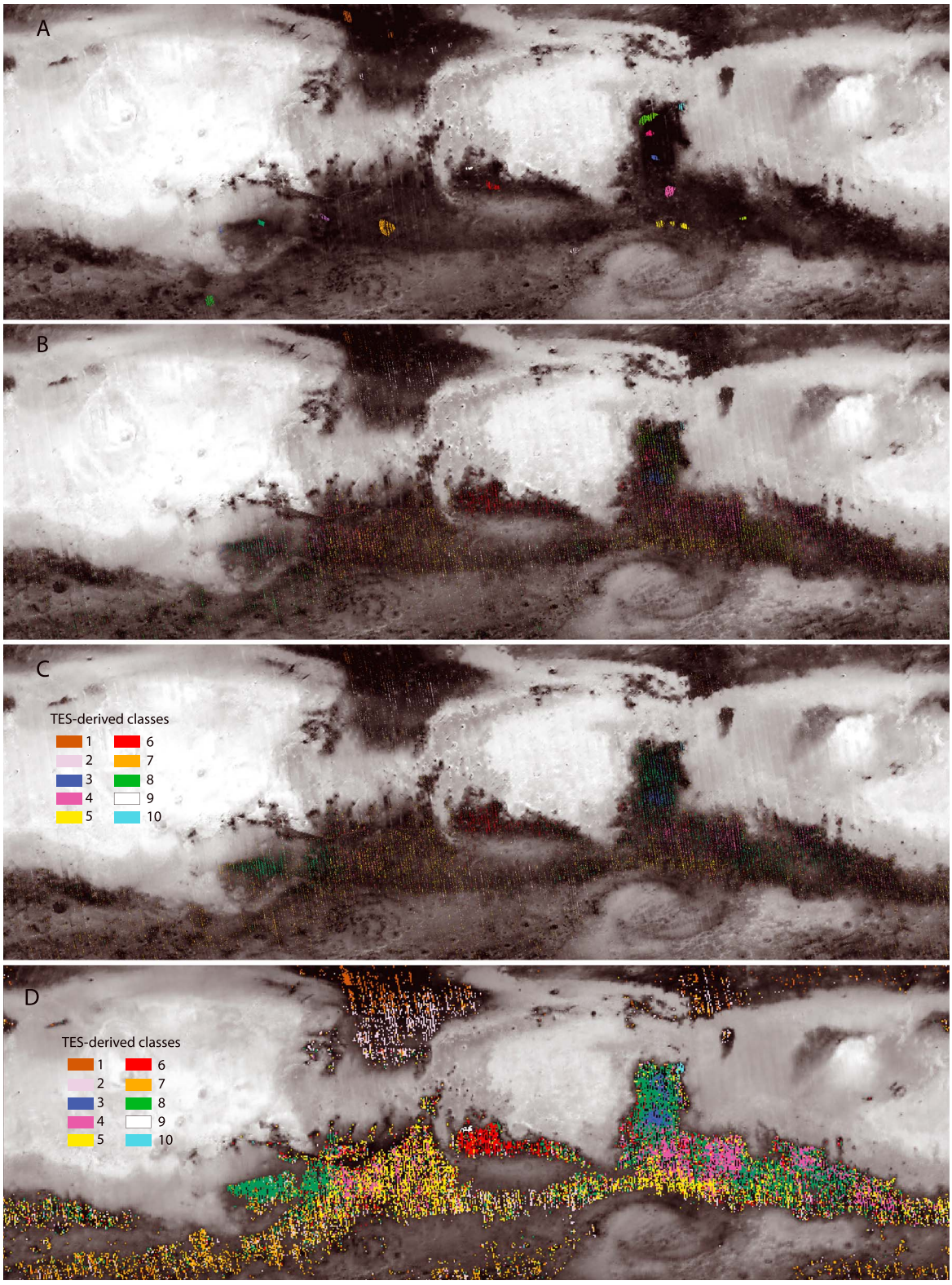

Figure 5. (a) Locations of 16 regions of interest (ROIs) on TES albedo map. (b) Results from maximum likelihood classification using 16 ROIs chosen from 1 sigma maps and IC analysis. Similarity between some class means resulted in merging of some groups. Results after merging are shown in Figure 5c. (c) Results after merging some classes shown in Figure 5b. The final number of classes is 10. (d) Class map from Figure 5c but degraded by a factor of four to a resolution of 2 ppd. This map was created by displaying the class occupying the most pixels in each 16 × 16 pixel square from Figure 5c. Some information from Figure 5c is lost; the intent is to help visualize the spatial distribution of classes in small print format.

Table 4. Class Mean Mineral Abundance and Standard Deviation (TES Derived)[a]

	Class 1		Class 2		Class 3		Class 4		Class 5		Class 6		Class 7		Class 8		Class 9		Class 10	
	N. Acidalia		S. Acidalia		Central Syrtis		Cratered A		Cratered B		Cratered C		Solis/ Aonium		Thaumasia/ Hesperia/ Syrtis		Meridiani Planum		Nili Fossae	
Feldspar	31	*5*	27	*5*	28	*3*	28	*4*	29	*5*	24	*4*	33	*5*	28	*3*	19	*3*	25	*6*
Low-Ca pyroxene	21	*4*	24	*4*	17	*3*	21	*4*	23	*5*	22	*4*	20	*4*	20	*4*	19	*3*	18	*4*
High-Ca pyroxene	3	*2*	2	*2*	15	*3*	10	*4*	6	*3*	7	*3*	4	*3*	10	*3*	4	*2*	9	*4*
Olivine	1	*1*	2	*2*	7	*2*	9	*2*	6	*3*	8	*2*	3	*2*	6	*2*	5	*1*	11	*5*
High-Si Phases	28	*4*	22	*4*	15	*2*	15	*3*	16	*4*	18	*2*	22	*4*	18	*3*	16	*2*	17	*4*
Sulfate	10	*3*	16	*4*	12	*2*	12	*3*	15	*4*	15	*3*	12	*3*	13	*2*	12	*2*	13	*3*
Hematite	4	*2*	2	*2*	1	*1*	1	*1*	1	*1*	2	*1*	3	*2*	2	*1*	22	*3*	2	*1*
Carbonate	3	*1*	2	*1*	4	*1*	3	*1*	3	*1*	3	*1*	3	*1*	3	*1*	2	*1*	4	*1*
Quartz	0	*<1*	0	*<1*	0	*<1*	1	*<1*	1	*1*	1	*<1*	0	*<1*	1	*<1*	0	*<1*	1	*1*
LCP: (LCP + HCP)	0.9		0.9		0.5		0.7		0.8		0.8		0.8		0.7		0.8		0.7	
Mapped age (%N/%H/%A)[b]	19/67/20		48/30/21		11/86/3		70/24/6		66/25/9		69/23/8		52/37/11		43/50/6		100/0/0		63/28/9	

[a]Italics indicate one standard deviation about the mean.
[b]%Noachian/%Hesperian/%Amazonian.

boundaries between classes are not as clear; for example, between Classes 4 and 5, and between Classes 5 and 6. Close inspection of the transition regions between these classes shows a high degree of heterogeneity and, in some cases, there is no obvious correlation with large-scale geomorphology or terrain age. Given the very subtle distinction in composition between these two classes, and the probable influence from local-scale heterogeneity in these heavily cratered plains, it is not surprising that the boundaries are unclear. These subtle distinctions are the least certain. However, as described in section 4.1, there does appear to be some corroboration in the divisions from VNIR data.

3.3.1. Classes 1 and 2—Northern and Southern Acidalia

A marked difference between northern and southern Acidalia modeled compositions is present at approximately ~45°N latitude, with southern Acidalia exhibiting higher-sulfate and lower high-silica abundances than northern Acidalia (Table 4). A spectral and visible albedo difference was also noted across this boundary by *Farrand et al.* [2000], *Dobrea et al.* [2003] and *Rogers et al.* [2007]. But because southern Acidalia exhibits a slightly lower spectral contrast than other low-albedo surfaces, *Rogers and Christensen* [2007] excluded it from their class map and did not discuss the mineralogical differences. However, broad correlation with a morphological boundary (discussed in section 5.1) suggests that the spectral and mineralogical difference is not simply related to thin dust cover. Geological processes that may have given rise to this compositional boundary are discussed in section 5.1.

Rogers and Christensen [2007] found that Solis Planum and some southern high-latitude surfaces were compositionally similar to northern Acidalia, and grouped Solis Planum and southern high-latitude units into RC Group 1 (Figure 1). All of these regions do exhibit relatively high abundances of high-silica phases [e.g., *Bandfield*, 2002] (this work, Table 4); however, in this work, we find that Solis Planum and low-albedo surfaces south and west of Thaumasia Planum exhibit slightly higher feldspar and lower high-silica phase abundance than the northern plains units and fall into their own class (Class 7). Given the different geologic setting and large spatial separation between this region and the northern plains units, it is not surprising that these units would be distinct in the multivariate analysis. In a detailed regional study of VNIR spectral characteristics, *Salvatore et al.* [2013] also found a distinction between Solis Planum and Northern Acidalia. Though Class 1 is largely confined to northern Acidalia, Class 2 does include many southern high-latitude surfaces and has a more scattered distribution.

3.3.2. Class 3—Central Syrtis Major

In the work of *Rogers and Christensen* [2007] Syrtis Major was globally distinct, forming its own group (RC Group 2), with most of the area of Syrtis Major being classified into that group (Figure 1). In this work, we find that Syrtis can be divided into two units. Areas in north central and south central Syrtis Major exhibit higher abundances of high-Ca pyroxene relative to areas around the periphery and in the west central portions of the shield. This new compositional boundary observed in the thermal infrared corresponds remarkably well with spectral distinctions made in a recent Syrtis mapping effort by *Clenet et al.* [2013] using OMEGA VNIR data.

3.3.3. Classes 4–6—Ancient Terrains in Cimmeria, Meridiani, and Tyrrhena

The ancient highland terrains, which were largely mapped as RC Group 3 [*Rogers and Christensen*, 2007], exhibit three subunits (Classes 4–6) in this work. Though all three classes are found throughout the heavily cratered terrains in the highlands, there are regions where each class is more prevalent. Class 4, found most commonly in Tyrrhena Terra and Cimmeria Terra, exhibits slightly higher high-Ca pyroxene and olivine abundance and lower sulfate abundance relative to Class 5, and higher feldspar/lower sulfate abundance relative to Class 6. Class 5 is found around the northern rim of Hellas Basin (within the outer basin ring, using a basin-centered radius of ~1600 km [*Wichman and Schultz*, 1989]), and in portions of western Noachis Terra. It exhibits elevated LCP abundance, and lower olivine and HCP abundance, compared to cratered terrains in Class 4. Last, Class 6 is found primarily in Sinus Meridiani, south of the hematite-rich area in Meridiani Planum. It is characterized by relatively low feldspar abundance, and high-sulfate and high-silica phase abundance, compared to Classes 4 and 5. The differences between these two classes are smaller than the typical differences between classes. In fact, if only single mineral groups are considered, they are not readily distinguishable from one another. However, it is the combination of mineral characteristics (e.g., for Class 6, the low feldspar plus high sulfate and high, high-silica phase abundance) that make the classes distinct when using multivariate methods.

3.3.4. Class 7—Solis Planum, Terra Sirenum, Aonium Planum

Class 7 consists of two merged classes from the original maximum likelihood classification. This class is distinguished by relatively high feldspar and high-silica phase abundance, and low olivine and pyroxene abundances, compared to other highland units. Found primarily in low-albedo regions south and west of the Thaumasia rise (Terra Sirenum), this class is relatively dispersed compared to some of the other classes. As described in section 3.1, spatially coherent areas of unique mineral abundance are relatively absent from this particular region. Solis Planum is a type locality for this class.

3.3.5. Class 8—Thaumasia, Protei Regio, Hesperia, and Outer Syrtis Major

Class 8 is the largest class, consisting of four merged classes from the original maximum likelihood classification. Class 8 surfaces are very similar to Class 4 in mineralogy; however, Class 8 surfaces exhibit slightly lower olivine and higher-sulfate abundances and are broadly associated with Hesperian volcanic provinces in the highlands. This class is dominant in Thaumasia planum, Protei Regio, Hesperia Planum, and the "outer" portions of Syrtis Major. It is also found in portions of the older, more heavily cratered terrains of Tyrrhena and Cimmeria Terra.

3.3.6. Classes 9–10—Meridiani Planum and Nili Fossae

The last two classes are confined to unique, small locations in the highlands and were already known to be distinct based on previous studies. Class 9, located in Meridiani Planum, exhibits a strong enrichment in crystalline hematite (>20%) compared to other regions [*Christensen et al*., 2000, 2001] (Table 3). The hematite enrichment in this region [*Christensen et al*., 2000] was the primary driver for its selection as a landing site for the Mars Exploration Rover (MER) *Opportunity* [*Golombek et al*., 2003], which landed in 2004; the mission is still active as of the time of this writing. *Opportunity* discovered and explored an expansive exposure of sulfate- and silica-rich sandstones, overlain by a deposit of hematite-rich spherules. The body of literature describing *Opportunity* results is extensive; the reader is referred to chapters within *Bell* [2008] as a starting point.

Class 10, located in Nili Fossae, exhibits a strong enrichment of olivine associated with relatively high thermal inertia material [*Hamilton and Christensen*, 2005]. The unit is cut by a system of graben related to the adjacent Isidis basin and overlies heavily altered clay-bearing units [*Ehlmann and Mustard*, 2012]. The olivine-rich unit has been interpreted as olivine-bearing lava flows as well as impact melt from the Isidis impact event [*Hamilton and Christensen*, 2005; *Mustard et al*., 2007].

4. Comparisons With Other Data Sets

Comparisons with other data sets serve two purposes: (1) they can serve to validate the more subtle compositional distinctions between some classes by revealing corresponding distinctions in independent data sets and (2) they help us understand potential relationships between surface mineralogy, upper meter elemental composition, and geomorphology. In the following sections, we present interclass comparisons with: VNIR spectral parameters designed to map olivine and pyroxene, element mass fractions, surface ages, and valley network density. Interpretations and implications derived from these comparisons are discussed in section 5.

4.1. Compositional Data Sets

4.1.1. CRISM and OMEGA Olivine and Pyroxene Distributions

The VNIR spectral region is used to measure solar reflectance from the upper few microns of a surface. It differs from the TIR spectral region in that (1) it is primarily only sensitive to Fe-bearing minerals, carbonates, and hydrated/hydroxylated phases and (2) the materials to which this wavelength region is sensitive do not combine spectrally in proportion to their abundance due to very low absorption coefficients [e.g., *Gaffey et al*., 1993]. Thus, VNIR spectroscopy is able to detect these materials even if present in low abundance, but the abundances cannot be easily quantified. For VNIR imaging spectrometer data, mineral detections are commonly mapped using spectral band indices that quantify the depth, width, and/or slope of diagnostic spectral features for that mineral [e.g., *Clark and Roush*, 1984; *Pelkey et al*., 2007]. Global data sets from two VNIR instruments are used here: one is the European Space Agency Mars Express Observatoire pour la Minéralogie, l'Eau, les Glaces, et l'Activité (OMEGA) instrument, and the other is the NASA Mars Reconnaissance Orbiter Compact Reconnaissance Imaging Spectrometer for Mars (CRISM) instrument. Both instrument teams have produced spectral parameter maps for key Fe-bearing minerals such as olivine, low-Ca pyroxene (LCP), and high-Ca pyroxene (HCP) [*Mustard et al*., 2005; *Poulet et al*., 2007; *Ody et al*., 2012].

CRISM operates in both a full spatial and spectral resolution targeted mode for coverage of key sites, as well as a lower spatial and spectral resolution, multispectral (MSP) mode for global-scale mapping [*Murchie et al*., 2007; *Seelos et al*., 2011]. The MSP data are collected for 72 channels between ~0.3 and 3.9 μm. Spectral parameters derived from these MSP images are available from the Planetary Data System in the form of 5° × 5° map tiles at a resolution of 256 ppd. We note that these map tiles are a first-order product and, while useful, have not yet been optimized to put the highest quality observations in the top layer. Thus, the quality of the mineral detections is uneven within each map tile. Some of the parameters are also subject to artifacts related to atmospheric conditions. However, the map tile products provide the best spatial coverage, and some of the parameters (described below) are less affected by these issues. In this work, the olivine index, LCP index, and HCP index map tiles were degraded to a spatial resolution of 8 ppd for direct comparison to the TES-derived mineral assemblage map derived in this work (Figure 6). Other parameters, such as the 1.9 μm hydration band and the 2.3 μm hydroxylation band, show extreme variability within the map tiles that is related to atmospheric variation and/or poor data quality, and thus, we did not use them in this global study. Global olivine and pyroxene spectral parameter maps were derived from OMEGA data at a resolution of 40 ppd by *Ody et al*. [2012] and are available from the European Space Agency's Mars Express mission data archive. *Ody et al*. [2012] calculated a pyroxene parameter and three olivine parameters ("OSP1," "OSP2," and "OSP3"), which are sensitive to differing olivine compositions and/or grain size and/or abundance.

For TES Classes 1–8, we retrieved CRISM and OMEGA index values and created histograms for these classes (40 bins, normalized for all bins, including zeros but not null values, Figure 7). Visual comparison of the CRISM (Figure 6) and OMEGA mafic parameter maps and the TES-derived class map show that Syrtis Major, Acidalia, and Thaumasia exhibit the same broad distinctions in all data sets. For a more quantitative comparison of all classes, we used a nonparametric test of statistical significance, the Mann-Whitney test, to determine whether the CRISM parameter distributions within each TES-derived spectral class are statistically distinct. This test determines the probability that two nonnormal populations of varying size have equal medians [*Burt et al*., 2009]. Despite the differences in sensitivities and linearity in spectral mixing between the VNIR and TIR ranges, there is remarkable agreement between the interclass trends exhibited in VNIR-derived mineral parameter values and the TES-derived mineral abundances. TES-derived compositional units with the most extreme mineralogical variations clearly correspond with extreme mineralogical variations in CRISM data (e.g., Syrtis Major is distinct from Acidalia, for example) (Figure 6). However, even the more subtle compositional distinctions, for example, Classes 4–6, the cratered terrain classes, show distinct distributions in CRISM-derived parameter values at the $\alpha \gg 0.99$ confidence level ($p < 0.0001$). For example, Class 4, which is slightly enriched in olivine and HCP relative to Classes 5 and 6, shows slight enrichments in olivine and HCP in CRISM data. Class 5, which is distinguished from Class 6 by lower olivine abundance, also shows lower olivine parameter values in CRISM and OMEGA data. What is especially remarkable is that the TES-derived differences between the class means are only at the 2–3% level (Table 4) but those differences are corroborated by an independent technique.

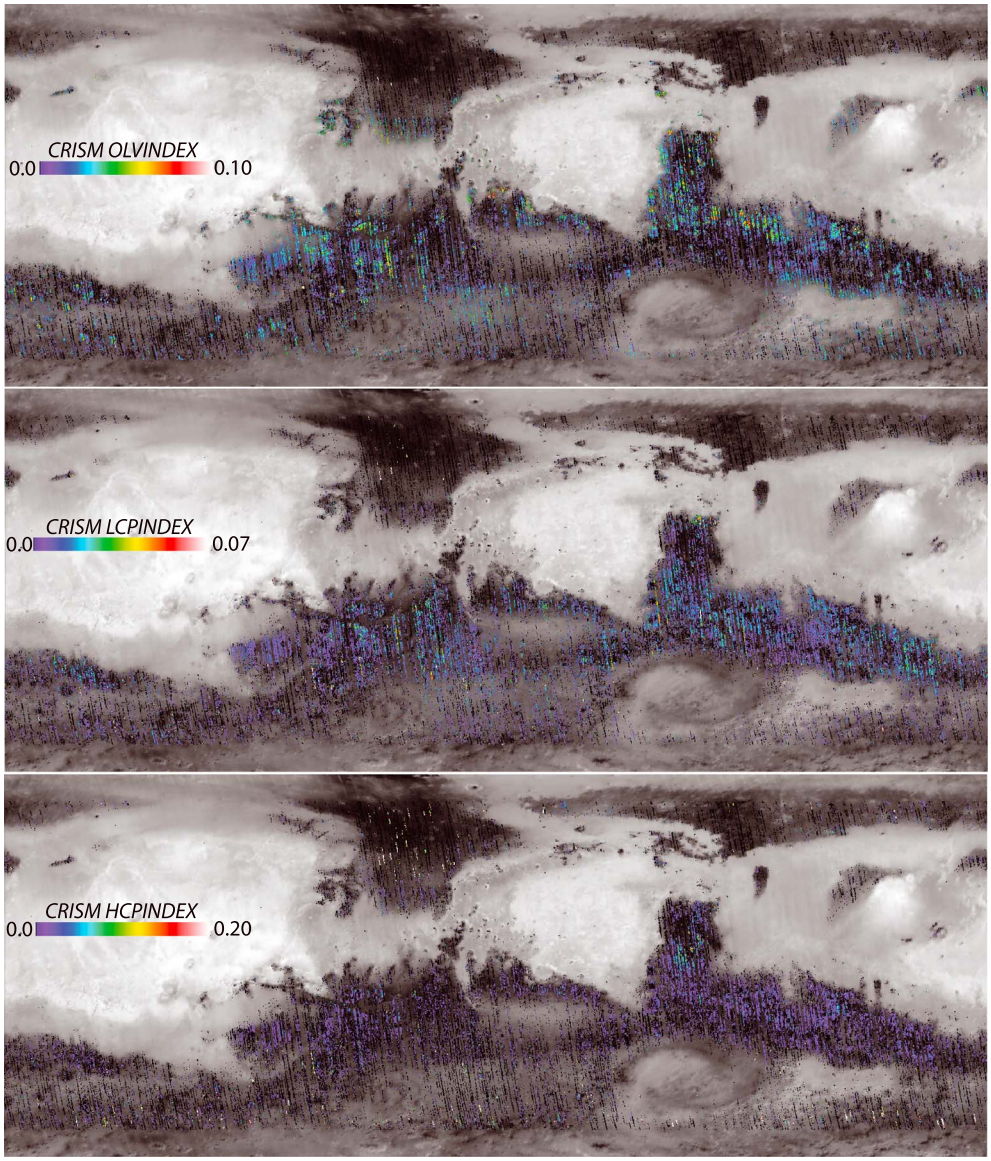

Figure 6. Spectral parameter maps for (top) olivine, (middle) low-Ca pyroxene, and (bottom) high-Ca pyroxene derived from CRISM MSP mosaic data. The parameter maps were degraded to 8 ppd and masked using the same mask applied to the TES mineral maps in this work. The parameter maps are overlain on TES albedo.

One exception to this relates to olivine abundance in Class 3. The class with the highest TES-derived olivine abundance (besides Nili Fossae, Class 10) is Class 4, which is found in the highlands and is a mix of Noachian- and Hesperian-aged surfaces. Compared to this class, Syrtis Major (Class 3) exhibits slightly lower olivine abundance. This result is not reflected in the CRISM- or OMEGA-derived olivine distributions [e.g., *Ody et al*., 2012]; rather, Class 3 shows the highest OLVINDEX values and number of olivine detections in CRISM and OMEGA data, respectively (Figure 7). The reason for this discrepancy is not clear; however, it likely relates to the differences in mineral assemblage between the different classes, which can affect the band depths/shapes in the region of olivine absorptions [e.g., *Horgan et al*., 2014].

4.1.2. GRS Elemental Abundance

Gamma ray spectroscopy is based on emission of gamma rays through cosmic particle interactions with nuclei and through radioactive decay. The wavelength of these interactions is dependent on the element; thus, by measuring the gamma ray intensities as a function of wavelength, elemental mass fractions can be determined. This technique is sensitive to the upper ~ one meter of material [*Boynton et al*., 2004]. The Mars

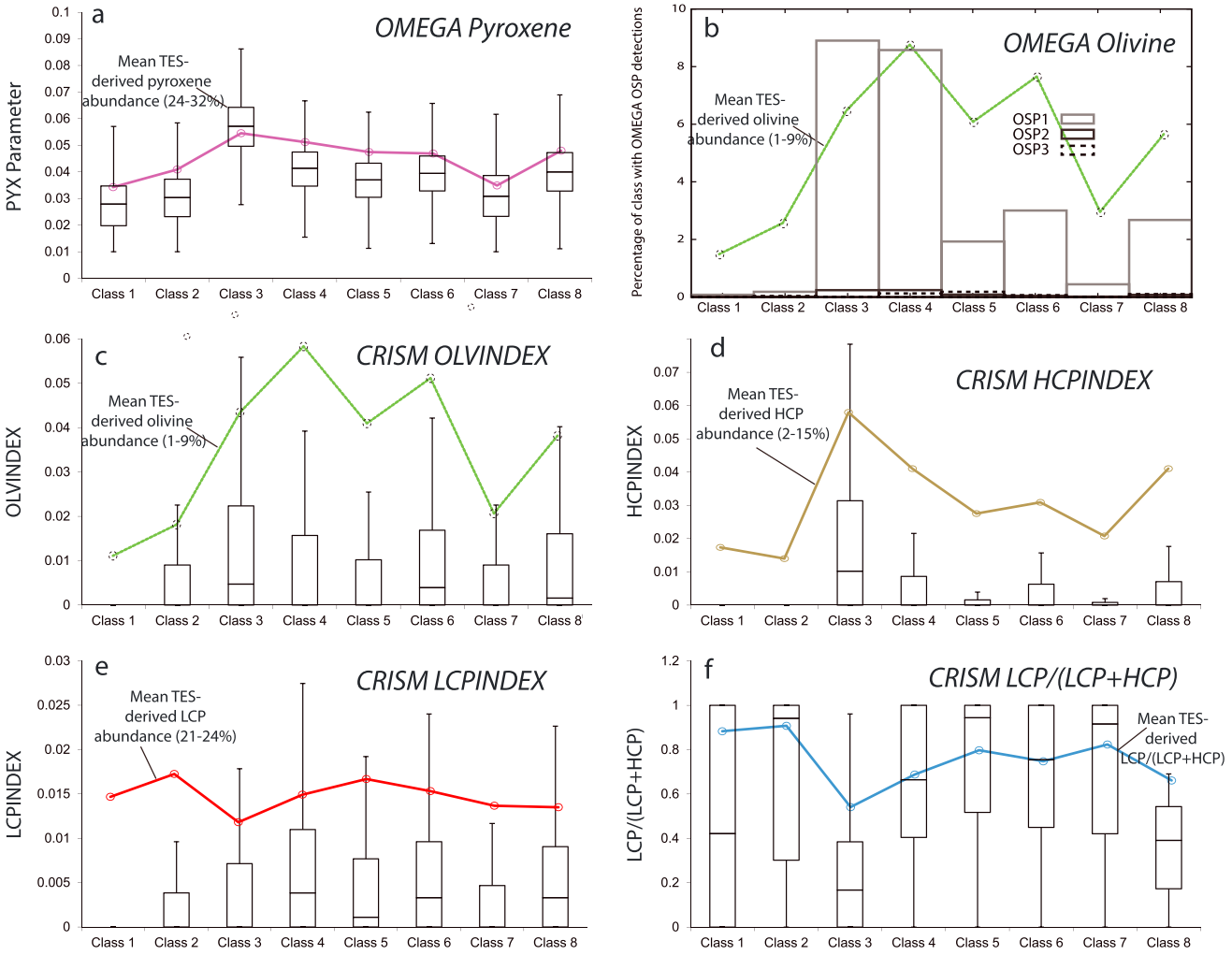

Figure 7. CRISM and OMEGA spectral parameter values for TES-derived Classes 1–8. (a and c–f) The bottom and top boundaries of each box represent the 25th and 75th percentile values, respectively, and the horizontal line through each box represents the median value. The whiskers represent the value at 1.5 times the interquartile range (75th–25th percentile). (b) OMEGA-derived olivine parameters constitute such a small fraction of each TES class that they were plotted as percentage of TES class with positive detections rather than spectral parameter box plots. For all plots, the colored line represents the mean abundance value for each TES-derived class, from Table 4. Pyroxene spectral parameter values derived from OMEGA data by *Ody et al.* [2012] are shown in Figure 7a. Percentage of each TES class with olivine detections from OMEGA data are shown in Figure 7b. Olivine spectral parameters OSP1, OSP2, and OSP3 are from *Ody et al.* [2012]. Olivine, high-Ca pyroxene, and low-Ca pyroxene spectral parameter values derived from CRISM multispectral survey data are shown in Figures 7c–7e. (f) Low-Ca pyroxene/total pyroxene ratios derived from CRISM LCP and HCP parameter maps.

Odyssey Gamma Ray Spectrometer (GRS) instrument suite measured elemental abundances for H, Th, K, Fe, Si, and Cl at very coarse spatial resolution (5 × 5° pixels) [*Boynton et al.*, 2007]. These maps (downloaded from the GRS website (http://grs.lpl.arizona.edu/specials/)) were generated by smoothing 2° raw concentration data with a 10° box car filter and then rebinning the filtered data at a resolution of 5° per pixel [*Boynton et al.*, 2007]. Previous studies have examined elemental properties as a function of geographical region [*Karunatillake et al.*, 2006, 2009; *Gasnault et al.*, 2010; *Taylor et al.*, 2010; *Baratoux et al.*, 2011] or terrain age [*Hahn et al.*, 2007]. This study complements those previous efforts by looking exclusively at low-dust regions with known mineralogical differences.

To compare TES maps with this lower resolution data set, we masked the GRS element mass fraction maps using the same mask we applied to the TES data (Figure 8). We then extracted element mass fractions for each pixel in each TES-derived compositional class and plotted these as histograms with 20 bins per population (Figure S1 in the supporting information). To permit a comparison of elemental characteristics within each class to the global characteristics, we need element mass fractions from the masked global

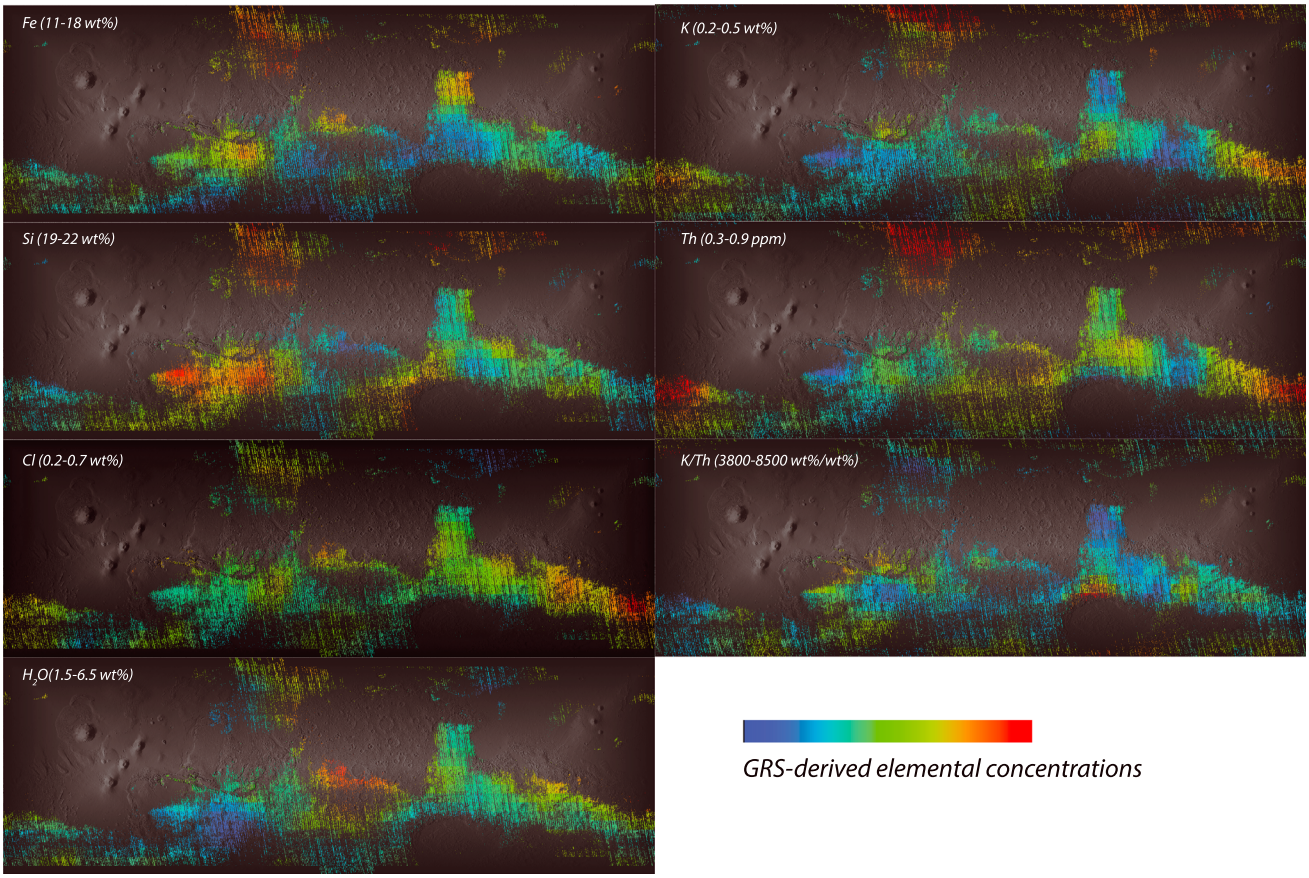

Figure 8. GRS distributions from *Boynton et al.* [2007], masked using the same mask applied to the TES mineral distributions and overlain on Mars Orbiter Laser Altimeter (MOLA) data.

concentration maps. However, the global population is much larger in size than the TES classes. To create a globally representative population of identical size to each TES-derived class, a spatially random selection of pixels from the global population was used for comparison (Figure S1). To simplify the presentation of these histograms, the GRS elemental distributions within each TES class are also shown in Figure 9. There, we first standardized the GRS elemental values by subtracting the global mean (calculated from the random, masked population, which excludes mantled surfaces) and dividing by the standard deviation. The plot shows the median and interquartile range standardized values for each class, which gives a sense of how the GRS characteristics within each TES class compare to the global mean. However, we note that many of the GRS distributions within each TES class are bimodal, skewed, or otherwise non-Gaussian, and these characteristics are not well captured in Figure 9. Using the full distributions (Figure S1) helps to better visualize the interclass differences as well as the differences between the classes and the global population. Figures 9 and S1 show that some classes are enriched or depleted in certain elements compared to a random population, whereas some classes are not distinct from random. Though some classes are not statistically distinct from the global population, they are distinct from one another (Figure S1), as described below.

TES-derived Class 1 shows strong enrichments in Si, Fe, K, and Th, compared to the global population and to the other classes, and moderate enrichment in H_2O. Class 2 shows similar trends to Class1 (except for Fe), but the enrichments are not as strong. Class 3, located primarily in central Syrtis Major, shows much narrower histogram peaks compared to the random population, due to a relatively small surface area and homogeneous elemental characteristics within this class. Of note for this class are the enrichment of Fe and depletion of K compared to cratered terrains just to the south (Classes 4–5). Similar elemental distinctions are observed in Hesperia Planum, a volcanic shield and plains of similar age and size.

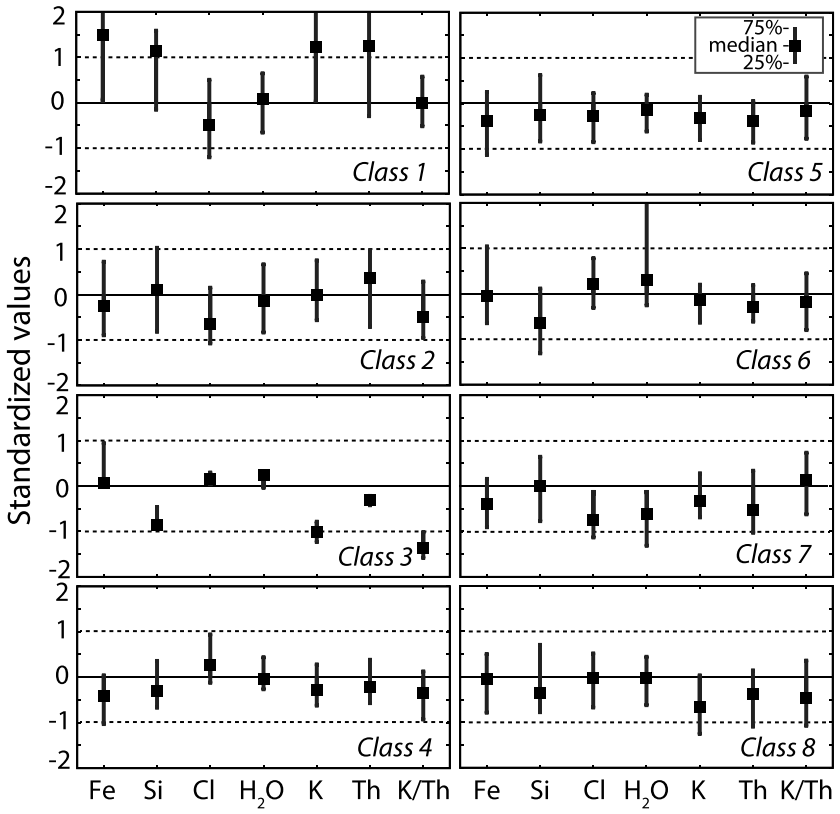

Figure 9. GRS elemental distributions from each TES-derived compositional class. GRS elemental values were first standardized by subtracting the mean of the global population and then dividing by the standard deviation [after *Karunatillake et al*., 2006; *Gasnault et al*., 2010; *Taylor et al*., 2010]. The global population is a spatially random selection of pixels of equal size to each TES class, and with the same data mask applied to the TES data (e.g., mantled surfaces are excluded). Black squares represent the median standardized elemental value from GRS data within each TES class. Gray vertical lines show the 25–75% percentile of standardized elemental values from GRS data within each TES class. GRS values for Classes 9–10 were not calculated due to the small size of these two classes. Note that many of the distributions are bimodal or skewed; to see the full distributions, as well as how each class compares to the other, please see Figure S1.

Class 4 appears slightly depleted in Fe and slightly enriched in Cl compared to the global population (Figure S1); compared to Classes 5 and 6, which are the other classes dominated by heavily cratered surfaces, it is perhaps slightly enriched in Cl compared to Class 5 and depleted in Fe compared to Class 6. Class 5 is remarkably similar to the global population. Class 6 exhibits higher Fe and Cl concentrations, and lower Si concentrations than the global population. It also appears to have a bimodal H_2O concentration (Figure S1), with particularly high H_2O abundances in Sinus Meridiani (Figure 8). Unmasked GRS element distributions show high H_2O concentrations associated with three large, high-albedo, low thermal inertia regions covering the Tharsis rise, Elysium Planitia, and Arabia Terra [*Boynton et al*., 2007]. These regions have been interpreted as having a relatively thick dust cover [e.g., *Christensen and Moore*, 1992]. We considered the possibility that the high H_2O concentration in Sinus Meridiani, compared to other low-albedo regions, is an artifact of being the southernmost extension of the Arabia Terra dust deposits. However, the H_2O enrichment in Sinus Meridiani extends ~20° southward of the margin of the Arabia dust unit. Thus, we conclude that the high H_2O concentration in Sinus Meridiani is likely indicating a surface source that is independent of the global dust unit.

Class 7, found dominantly in Solis Planum (western Thaumasia Planum) and Aonium Planum, is enriched in Si compared to other highlands, Classes 4, 6, and 8, and depleted in Cl, H_2O, and Th relative to the global population (Figures 8, 9, and S1). For Class 8, found dominantly in Thaumasia Planum, Protei Regio, Hesperia Planum, and portions of Syrtis Major, the Si and Th element concentration distributions appear bimodal (Figure S1); this is likely due to the relatively large size of this class and the fact that it occurs in multiple

terrains separated across the globe. Using the spatial distributions in Figure 8, we can see that among Class 8 surfaces, Si is highest in Thaumasia Planum and Protei Regio, Th is lowest in Hesperia and Thaumasia Planum, and slightly less depleted in Syrtis Major and Protei Regio, and Fe is intermediate to high in all four regions. All four of these regions exhibit relatively low K concentrations (Figure 8); this is reflected in the lower histogram peak value relative to the global population (Figure S1). Thus, although the areas mapped into Class 8 are mineralogically similar, in terms of grouped mineral abundance, there is moderate geochemical variability (1–2 wt % for Fe and Si, $<$0.2 ppm for Th) within this class. These variations are clustered to specific geographic areas and are likely due to variations in individual mineral species between regions. In addition, in Syrtis Major, the GRS footprint is large enough to be influenced by both compositional classes that are present there (Classes 3 and 8), thereby affecting the measured elemental abundances.

Global compositional characteristics were generated from GRS data alone, using various statistical techniques, by *Gasnault et al*. [2010], *Karunatillake et al*. [2009], and *Taylor et al*. [2010]. Gasnault et al. applied principal components and clustering analysis to GRS-measured distributions of H, Cl, Fe, Si, K, and Ca and showed that there are at least five chemically homogeneous clusters using these inputs. They found significant differences between Acidalia and the low-dust portions of the cratered highlands, as we did with TES data, and also observed heterogeneity within the mantled portions of the highlands, which were excluded from our study. *Karunatillake et al*. [2009] identified statistically significant Gaussian "tails" (e.g., pixels above/below 1 standard deviation from the mean) of each element distribution and delineated "chemically striking regions" from areas that were in the Gaussian tails for two or more elements. They used GRS-measured distributions of H, Cl, Fe, Si, K, Th, Ca, and Al. Note that, rather than classifying all bins, this method identifies regions that are chemically distinct from the global average. A visual comparison between our Figure 5d and their Figure 3 shows some similarity in the Thaumasia/Solis Planum region, where a chemical distinction was observed between the two regions. They also observe a difference between northern and southern Acidalia, but the boundary is shifted slightly to the north of where we observe a mineralogical difference. If a mineralogical phase (rather than oxidative weathering, section 1) is responsible for the observed spectral difference between northern and southern Acidalia, the difference in boundary locations between our study and that of *Karunatillake et al*. [2009] may represent a transition in depth of the responsible phase. *Taylor et al*. [2010] used a K means clustering technique on the GRS-measured Fe, Si, K, Th, and Ca distributions; they excluded the volatiles H and Cl from their analysis, in an effort to focus on igneous chemical variability. Taylor et al. found six chemically distinct clusters. One cluster was considered "average Mars"; the other clusters showed enrichment or depletion in at least one element relative to average Mars.

In Figure S2 and Table S1, we show a detailed comparison of our mineralogical classification with the chemical classification map produced by *Taylor et al*. [2010]. Of the three complementary GRS-based classification studies described above, we focus on the Taylor et al. study because all pixels were classified, allowing for a more direct comparison with our results. The *Taylor et al*. [2010] classification, masked to exclude mantled surfaces in the same manner as the TES data, shows many similarities to the mineralogy-based classification. The northern lowlands are chemically and mineralogically distinct from the highlands, with large percentages of TES Classes 1 and 2 (71% and 36%, respectively) found within the Taylor et al. GRS Class 6, but the difference in mineralogy between northern and southern Acidalia is not reflected in the chemical data (though it was recognized by *Karunatillake et al*. [2009], who used different methods, discussed briefly above). The GRS-based class map of *Taylor et al*. [2009] also shows chemical similarity between Syrtis Major, Hesperia Planum, and portions of Thaumasia Planum (the highland Hesperian volcanic terrains), which are mapped as GRS Class 3. Large percentages of TES Classes 3 and 8 (85% and 32%, respectively) coincide with GRS Class 3 (Table S1). However, within Thaumasia, the GRS classification shows chemical divisions that were not observed in the mineralogical-based classification (Figure S2). The GRS-based map also shows Sinus Meridiani as chemically distinct from average Mars (GRS Class 4) and adjacent low-dust terrains, as we do in the mineralogical data with TES Class 6. Sinus Meridiani is mapped as GRS Class 2, which is depleted in Ca relative to average Mars. GRS Class 2 comprises the largest percentage (38%) of TES Class 6, which is characterized by relatively low abundance of feldspar and higher abundance of sulfate and high-silica phases, suggesting that the lower abundance of feldspar could be responsible for the lower Ca in this region. GRS Class 2 is also found in portions of the relatively unmantled highlands that do not correspond with TES Class 6, highlighting the importance of both mineralogical and chemical data sets for interpreting surface materials. For example, low abundance of feldspar may drive the low-Ca abundance in Sinus Meridiani, but pyroxene composition and/or

abundance may drive the low-Ca abundance elsewhere within GRS Class 2. TES Classes 5 and 7 are dominantly made up of GRS Class 1, which comprises 41% and 66% of those TES classes, respectively. GRS Class 1 is relatively depleted in Fe and Ca compared to average Mars. Last, GRS Class 5, which is enriched in Ca relative to average Mars, is found primarily in low-spectral contrast regions (which are dust covered at scales of millimeter to centimeter) that were excluded from our study. Thus, it is difficult to assess the mineralogical composition of that class. To conclude, the GRS-based classification shows not only notable similarities to the mineralogical classification but also some differences. The GRS-based classification was (necessarily) generated from limited elemental information; with limited variables, it is not possible to discern subdivisions that may be present within classes. Second, the GRS-based classification was generated from data over both mantled and low-dust regions [*Taylor et al*., 2010], representing a fundamentally different population contributing to global statistics than was used in our study. Both of these factors certainly play a major role in the differences between the two classifications.

4.2. Geomorphological Data Sets

4.2.1. Apparent Surface Age

Although we have described broad geographical associations with each TES-derived class, we also determined the proportions of each class found in Noachian-, Hesperian-, and Amazonian-aged terrains (Table 4). We used the mapped apparent ages from the U.S. Geological Survey 1:15 M Miscellaneous Investigation Series (maps I-1802A-C) [*Scott and Tanaka*, 1986; *Greeley and Guest*, 1987; *Tanaka and Scott*, 1987]. Units with transitional ages, which cover a small area (<5%) on the surface, were excluded from our analysis [e.g., *Hahn et al*., 2007].

Most Amazonian-aged surfaces are dust covered and therefore were excluded from the TES data analyses (section 2.1). Classes 1–2 are the only classes with a significant proportion of Amazonian-aged surfaces (~20%). Class 3 is strongly associated with Hesperian-aged surfaces (86%). Classes 4, 5, 6, 9, and 10 are found primarily in Noachian-aged surfaces (>63%). Classes 7 and 8 are found in approximately even proportions in Noachian and Hesperian-aged terrains (Table 4).

4.2.2. Valley Network Density

Valley networks on Mars provide a record of fluvial activity on the surface. The locations and density of networks vary across the planet [*Carr*, 1995; *Hynek et al*., 2010]; however, they are primarily restricted to late Noachian/early Hesperian surface ages [*Fassett and Head*, 2008]. The climate conditions and their durations required to form these channels are controversial. Arguments for climate conditions range from a wet, warm environment in which rainfall would have been supported over long durations [*Craddock and Howard*, 2002] to shorter pulses of precipitation activity [*Stepinski and Stepinski*, 2005; *Segura et al*., 2002]. Because fluvial action can result in both mechanical and chemical alteration of the surface, we compared drainage density to our TES-derived class map to determine whether any single class exhibits statistically distinct valley network density distributions. We calculated drainage density using the valley map of *Hynek et al*. [2010] by calculating the total valley length within a radius of 235 km, and plotting the values at a resolution of 8 pixels per degree (~7.5 km/pixel at the equator) (Figure 10). We masked the map using the same mask we applied to the TES data, for direct comparison. We extracted density values for TES-derived Classes 1–8 and plotted them as 17 bin histograms ranging from density values of 0.0 to 0.08 km^{-1} (Figure 11). Class 6 is distinct from other classes ($p < 0.0001$ using the Mann-Whitney test [*Burt et al*., 2009]) in that it exhibits a greater number of high-drainage density values (Figure 11) than the other classes. However, from this analysis alone, it is difficult to distinguish coincidence from cause. In the drainage density map (Figure 10), the transition from globally high values in Sinus Meridiani to globally intermediate values southwest of Meridiani (and out of Class 6) appears gradual, suggesting coincidence is more likely. Given that alteration mineralogic assemblage depends on the primary mineralogy (which could be variable) to some degree [e.g., *Tosca et al*., 2004], and also given the uncertainty about the duration of channel formation events, it is not surprising that a clear correlation between valley network density and TES-derived compositional classes is lacking.

5. Discussion

The methods we have used here have reinforced the original compositional boundaries described by *Bandfield et al*. [2000a], *Christensen et al*. [2000], *Hamilton et al*. [2003], *Hoefen et al*. [2003], and *Rogers and*

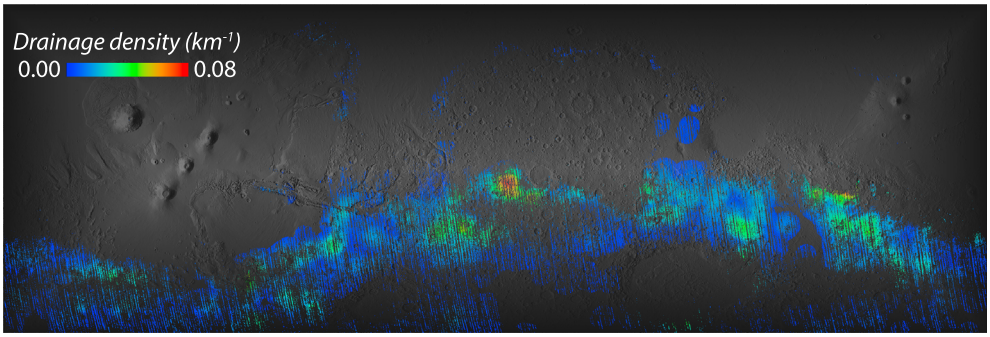

Figure 10. Valley network density, masked and overlain on MOLA-shaded relief. The data are from *Hynek et al.* [2010].

Christensen [2007] (section 3.3). Our TES-based results, integrated with CRISM, OMEGA, and GRS data, have also elucidated a number of new and important constraints on the compositional variability of the Martian surface. Below, we discuss these new constraints, organized by geographic region and geologic setting.

5.1. The Northern Lowlands

As described in section 1, the nature of the unique ST2 [*Bandfield et al.*, 2000a] signature of the northern lowlands remains enigmatic. Originally interpreted as a difference in igneous compositions, several researchers have reinterpreted the TES spectral characteristics of the lowlands to represent altered basalts through aqueous [*Wyatt and McSween*, 2002; *McLennan*, 2003; *Kraft et al.*, 2003], periglacial [*Kraft et al.*, 2010], and/or oxidative weathering processes [*Salvatore et al.*, 2013]. Others [*Karunatillake et al.*, 2006] argue on the basis of GRS K/Th data that the lowlands *do* contain a distinct igneous unit but that the Si concentration is not high enough for that unit to be andesitic in composition, as proposed by *Bandfield et al.* [2000a].

A previously reported [*Rogers et al.*, 2007], but somewhat underemphasized (section 3.3.1), TIR constraint on the nature of lowland surfaces comes from the observation that the lowlands may be divided into two compositional classes (Classes 1 and 2). Both are olivine and pyroxene poor, but they differ in modeled sulfate and high-silica phase abundance. Moving northward, the more sulfate-enriched class (Class 2) transitions to a high-silica phase dominated unit (Class 1) near ~45°N latitude. The spectral difference between northern and southern Acidalia was previously reported by *Farrand et al.* [2000], *Dobrea et al.* [2003], and *Rogers et al.* [2007]. But because the southern Acidalia region exhibits slightly lower spectral contrast, *Rogers et al.* [2007] suggested that the spectral shape may arise from mixing with dust and did not discuss the mineralogical differences between northern and southern Acidalia further. The southern Acidalia spectral shape was excluded from analysis in the companion paper by *Rogers and Christensen* [2007]. Here we reconsider these differences because, as noted by *Kraft et al.* [2010], this boundary roughly corresponds with a morphological transition between hummocky terrain and subdued hummocky terrain with polygonally patterned ground. *Kraft et al.* [2010] suggested that the boundary corresponds with the extent of

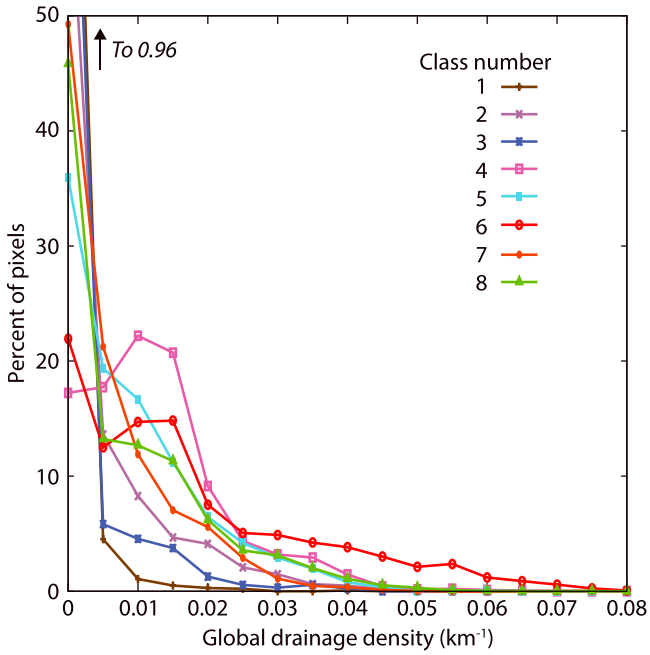

Figure 11. Valley network density values from the TES Classes 1–8.

periglacial activity in the north and that the spectral signatures arise from aqueous weathering and silica mobilization in ice-rich soils. Detailed studies of the morphological properties are clearly necessary to understand the nature of this distinct mineralogical boundary.

In a previous study using GRS data to evaluate compositional differences between the northern lowlands and southern highlands, *Karunatillake et al*. [2006] found statistically distinct differences in only K and Th. Differences in the other elements (e.g., Si and Fe) were not detected due to averaging what we now know are distinct compositions in the southern highlands (for example, Syrtis Major was grouped with Sinus Meridiani and other Noachian surfaces in that work). Here because we have split the highlands into multiple, distinct terrains, we are able to better observe elemental differences between the Noachian portions of the highlands, Hesperian highlands, and Hesperian lowlands and interpret those differences. For example, Figures 8 and S1 show that the lowlands (Classes 1–2, particularly Class 1) are enriched in Si compared to most highlands surfaces, excluding Thaumasia. The lowlands are also enriched in Fe compared to much of the Noachian cratered highlands (Classes 4–6). This Fe distribution was noted by *Taylor et al*. [2006] and was also reflected in a result by *Hahn et al*. [2007], who showed that Hesperian terrains (they did not separate Hesperian lowland and Hesperian highland surfaces) were statistically enriched in Fe compared to Noachian-aged surfaces.

The slightly higher sulfate abundance in Class 2 is difficult to interpret. Without supporting evidence from GRS (no S map is available), OMEGA, or CRISM (MSP parameters that map sulfate are highly variable with atmospheric conditions), we are reluctant to conclude that sulfate enrichment is truly present in southern Acidalia. It is worthwhile to note, however, that if the northern lowlands were a location for repeated groundwater emergence and evaporation [*Andrews-Hanna et al*., 2010], this process should have deposited sulfates and other salts. Though Cl abundance is not enriched in the northern lowlands compared to the global population (Figure 9), the values are comparable to Meridiani Planum and other areas of proposed groundwater evaporation (Figure 8).

5.2. Heavily Cratered Terrains of Dominantly Noachian Age

New subdivisions within the heavily cratered terrains of the highlands, which were previously largely mapped into a single group (RC Group 3) [*Rogers and Christensen*, 2007] (Figure 1), are now apparent (Classes 4–6). Though these classes are relatively scattered compared to others, there are two notable new constraints on the composition of heavily cratered highlands that we can discuss, with distinctive surface mineralogies concentrated in Sinus Meridiani and the northern Hellas basin rim.

Sinus Meridiani, the low-albedo region bordering the southern margin of the Meridiani Planum hematite unit, is compositionally distinct from similarly aged heavily cratered terrains. Its class (6) is characterized by higher-sulfate and high-Si phase abundance, and lower feldspar abundance than other low-dust surfaces on Mars (Table 4). We note that these characteristics are similar to those found in Class 9 (Meridiani Planum), once normalized for crystalline hematite abundance. The southern and western boundaries of this class are poorly defined because of the increasing dust cover in these directions, which obscures the underlying substrate. However, the compositional distinction in Sinus Meridiani is also present in GRS data (Figure 8), which is sensitive to a deeper volume, with some of the highest H_2O values in low-dust regions concentrated in this region. Sinus Meridiani also exhibits higher abundances of Fe (Figures 8 and 9). Together, the Fe, H_2O and TES sulfate abundances may point to a higher proportion of iron sulfates in the Sinus Meridiani soils. From these global-scale data sets, it is difficult to distinguish small-scale, highly elevated mineral concentrations common to a particular region from homogeneously distributed, regional-scale distinctions in lithology. Thus, it is possible that the higher-sulfate and high-silica phase abundance common to this region could be due to small, remnant sulfate-bearing layered terrains similar to those found in Meridiani Planum and investigated by the MER rovers [e.g., *Bell*, 2008]. The area does contain a few "hydrous mineral" detections from CRISM and OMEGA data sets [*Carter et al*., 2013]; however, the particular species of hydrous minerals were not specified for each location. Detailed, high-resolution studies of this region are needed to determine whether concentrated sulfate-bearing exposures are present. Alternative explanations for the elevated sulfate and high-silica phase abundances in this region include erosion and aeolian transport of sulfate-bearing sedimentary units from the north, or reworking/erosion of local sulfate-bearing units to leave a mixture of basaltic and sulfate-/silica-bearing evaporitic material. Though hydrology models using a homogeneous subsurface do not predict groundwater upwelling in Sinus Meridiani, a heterogeneous

subsurface could allow for groundwater upwelling and evaporation in this region [*Andrews-Hanna et al*., 2010], so such processes cannot be eliminated at this time.

A second notable new finding is that the northern margin of the Hellas impact basin is distinct from heavily cratered surfaces just outside the Hellas outer ring. Within the outer ring, Class 5 (a relatively olivine- and HCP-poor unit, Table 4 and Figure 7) is the spatially dominant class. The transition between HCP-poor surfaces (Class 5) to slightly more HCP-enriched surfaces (Classes 4 and 8), roughly corresponds with the outer ring of Hellas basin. The dominance of LCP along the Hellas northern margin might suggest that the surface materials were largely derived from LCP-dominant basaltic units. A difference in primary crustal compositions within and outside of a major impact basin is not unreasonable; also, local-scale outcrops of LCP-dominated (>50 vol %) lithologies have been observed in this region [*Rogers and Fergason*, 2011]. The transition between HCP-poor and HCP-rich surfaces also roughly corresponds with a change in K/Th ratio, such that areas within the Hellas outer ring exhibit very high K/Th ratios relative to regions outside the Hellas outer ring (Figure 8). *Taylor et al*. [2006] noted that K/Th ratios are high for the entire basin, which is not visible here due to the data mask applied. Both the basin floor as well as the concave up, basin-facing sloped terrain between the main basin scarp and the outer ring contain an abundance of layered sedimentary units [e.g., *Tanaka and Leonard*, 1995; *Malin and Edgett*, 2000; *Leonard and Tanaka*, 2001; *Moore and Wilhelms*, 2001; Crown *et al*., 2005; *Mest and Crown*, 2005; *Korteniemi et al*., 2005; *Moore and Howard*, 2005; *Wilson et al*., 2007], of which some are clay bearing [*Crown et al*., 2010; *Ansan et al*., 2011] and silica bearing [*Bandfield*, 2008; *Carter et al*., 2013]. Given that both the geomorphological and chemical evidence favors aqueous processes and alteration, an alternative explanation for the HCP- and olivine-poor mineralogy is that alteration processes may have preferentially weathered HCP and olivine from units whose primary compositions were similar to those found in Tyrrhena Terra (e.g., outside the outer basin ring). The local-scale observations of clay and silica-bearing units would also support this scenario.

5.3. Hesperian Highland Volcanic Provinces

There are three new findings from this work that clearly indicate Martian surface materials reflect changes in magma source compositions and igneous processes through time. First, Hesperian volcanic provinces in the highlands (Hesperia, Thaumasia, Protei Regio, and outer portions of Syrtis Major) largely fall into the same TES compositional class (Class 8), which is characterized by elevated HCP abundance compared to most of the highlands (Classes 5 and 6). Previous studies using local-scale observations of Hesperian and Noachian pyroxene-bearing surfaces have noted a trend of decreasing LCP/(total pyroxene) between Noachian and Hesperian terrains [*Mustard et al*., 2005; *Baratoux et al*., 2007; *Poulet et al*., 2009]. Our results build on their initial findings by confirming this trend on a larger scale. Not only do Hesperian highland volcanic provinces exhibit low LCP relative to ancient cratered terrains, but their overall bulk mineralogy exhibits relatively low olivine and higher plagioclase and HCP, on average, compared to the ancient terrains. Where high HCP is found in the ancient terrains, it is typically accompanied by relatively high olivine abundance (Class 4), as also noted by *Mustard et al*. [2005].

The decrease in LCP/(LCP + HCP) over time in Martian surface materials is consistent with thermodynamic models [*Baratoux et al*., 2013] that show primitive magmas derived from the mantle should show such a decrease with time, as a result of thickening of the lithosphere and cooling of the mantle. One discrepancy with these models concerns olivine, which should crystallize in abundances of 20–40 wt % for magmas produced throughout Martian history [*Baratoux et al*., 2013]. Neither VNIR nor TIR data sets support abundances of olivine this high for most terrains. One possible explanation is the preferential weathering of olivine under very low water-to-rock ratios [e.g., *Tosca et al*., 2004], which could produce poorly crystalline aluminosilicates, silica, and/or sulfates on rock/soil surfaces and in vugs and veins. High-silica phases and sulfate minerals are modeled at 10–20 vol % and 10–15 vol % levels, respectively, in TES data. Thus, if the crystallization products modeled by *Baratoux et al*. [2013] are correct, the "missing" olivine may be obscured or accounted for by high-silica phases and sulfates. Compelling spectral evidence for preferential loss of olivine at local scales through physical and chemical weathering has been presented by *Bandfield and Rogers* [2008] and *Bandfield et al*. [2011]. A second possibility for the missing olivine is that ancient magmas were Cl rich, which suppresses the crystallization of olivine [*Filiberto and Treiman*, 2009; *Ustunisik et al*., 2010]. A third possibility is that the Noachian surface materials were generated from low degrees of partial melting, which would also result in low olivine abundance; however, that would likely be inconsistent with the relatively high LCP/total pyroxene ratio observed in Noachian-aged units [*Baratoux et al*., 2013].

The second finding relates to the abundances of K and Th in Hesperian highland volcanic terrains relative to older highland terrains. *Baratoux et al*. [2011] showed that highland volcanic provinces of Hesperian age exhibit chemical similarity in Fe, Si, and Th abundance and are distinct from Amazonian-aged volcanic units in Tharsis and Elysium. Here we show that these Hesperian highland volcanic provinces are distinct from the cratered terrain classes (4–6), exhibiting relatively low K concentrations (Figure 8). Th concentrations are low to intermediate, depending on the region. One explanation for the decrease in K and Th concentrations between Noachian and Hesperian highland terrains is loss of incompatible elements after formation of the Noachian crust. However, an enrichment of K and Th in older terrains might suggest lower degrees of partial melting, which is inconsistent with the higher degrees of partial melting suggested by the relatively high LCP/total pyroxene ratios observed in the older terrains [e.g., *Baratoux et al*., 2013]. Alternatively, the higher K and Th in older terrains may be caused by magmatic differentiation, suggesting a more complex set of processes to build up the Noachian crust than simple changes in degree of partial melting with time. Though these areas are mineralogically similar in terms of modal abundance of major mineral groups, there is moderate ($<$2 wt %) geochemical variability in Si and Fe concentration within this class, with the variations clustered to specific geographic areas. Si is enriched in Thaumasia Planum and Protei Regio, but not Syrtis or Hesperia. However, as others have noted [*Boynton et al*., 2007], the total global variation in Si concentration is relatively modest, ranging from ~19 to 22 wt %. At least in Syrtis Major, some of the difference may be due to the fact that multiple classes (3 and 8) are present and likely influence the GRS measurements over both units.

The third new finding is that Syrtis Major may be subdivided into two classes. The central lavas (Class 3) exhibit slightly higher pyroxene/feldspar ratios relative to peripheral lavas (Class 8). Though the distinction is subtle, we note that the boundary corresponds remarkably well with spectral distinctions made in a recent Syrtis mapping effort by *Clenet et al*. [2013] using OMEGA VNIR data. CRISM HCP parameter distributions are also distinct between the two classes at $>$99% confidence level. The differences likely reflect changes in primary melt composition in this region. High-resolution maps of the eruptive history of Syrtis Major (such as the preliminary work by *Jodlowski et al*. [2013]) may reveal whether the compositional differences relate to different eruptive periods.

5.4. Broad Insights Regarding Compositional Provinces of Mars

Nearly all of the compositional boundaries apparent in the TES-derived class map are discernible in GRS elemental mass fraction data. This correspondence provides an indication of the minimum depth that these classes represent and suggests that igneous processes and large-scale sedimentary and/or glacial processes (e.g., Hellas basin fill, southern Acidalia outwash, northern Acidalia periglacial activity) are the primary control on spatial variations in composition. Though some of the mineralogical characteristics are likely reflective of surficial weathering processes (e.g., oxidative weathering [*Salvatore et al*., 2013] or episodic aqueous alteration, perhaps under thin transient films of water [e.g., *Kraft et al*., 2003; *Michalski et al*., 2005]), any secondary mineral assemblages that are present as thin coatings must be controlled by the underlying primary mineralogy.

Presently, a lack of clarity with respect to the modeled high-silica phase component (primary glass, secondary silica/opal, poorly crystalline silicates, and/or oxidative weathering, section 1) as well as the spectral mixing behavior of poorly crystalline hydrated materials, particularly in the NIR (which have weakened hydration bands compared to crystalline materials [e.g., *Cloutis et al*., 2008; *Milliken and Mustard*, 2005]) complicate assignments of lithology. Thus, the primary takeaway result from this work should be a spatial map of bulk compositional variation, rather than specific rock types or lithologies. That said, the remarkable agreement between the VNIR and TIR data sets does support some of the major compositional trends reported here and by others, with respect to variations in LCP/(LCP + HCP) ratios and olivine abundance.

Terrains that are distinct based on geomorphology and age tend to also exhibit distinct compositions. This supports the idea that the Martian surface layer (i.e., the upper few tens of microns of sediment and rock that influence spectral measurements [e.g., *Christensen and Moore*, 1992]) has not been globally homogenized by impact or aeolian processes. The notion of a globally uniform coarse-grained soil fraction arose from observed geochemical similarity of some low-sulfur (and presumably, low-dust) soils measured in situ at Gusev Crater and Meridiani Planum [*Yen et al*., 2005], and later, Gale crater [*Bish et al*., 2013]. At Gale crater, soil heterogeneity has been observed, with evidence of inputs from local rock sources [*Meslin et al*., 2013; *Cousin et al*., 2014]. However, because many of the Gale soil targets are chemically similar to those observed

at Gusev crater and Meridiani Planum, the notion of a "global" or "widespread" basaltic soil has persisted [*Bish et al*., 2013; *Meslin et al*., 2013]. Despite the chemical similarities at these three locations, the orbital data from the TES, OMEGA, CRISM, and GRS instruments do not support this hypothesis. One possible way to reconcile these observations is that these landing sites may have sampled similar units; this possibility can be assessed in a limited manner from results presented here. Gusev crater surfaces do not meet the data selection criteria used for this study (Table 1); however, Meridiani Planum (Class 9) and portions of Gale crater do. Although some pixels in and around Gale crater were not classified (using the methods described in section 3), the remaining pixels fall into Class 6 (most abundant), Class 4, and Class 8 (Figures 5c and 5d). As described earlier (section 5.2), Meridiani Planum surfaces, once normalized for hematite abundance, are very similar to the Class 6 mean composition. Thus, the TES data are in agreement with the similar soil measurements made by the *Opportunity* and *Curiosity* rovers at Meridiani Planum and Gale crater. However, the occurrence of other distinct units in the highlands (Figures 5c and 5d) does not support homogenization on a global scale.

6. Conclusions

Through statistical analyses of mineral abundance derived from the TES instrument and synthesis with GRS and CRISM data, we have made the following conclusions:

1. Feldspar, low-Ca pyroxene, high-silica phases, and sulfates are generally modeled above 10 vol % for nearly all TES pixels in low-dust regions. High-Ca pyroxene, olivine, and hematite are modeled above the 10% level for many regions; conversely, modeled abundances of zero are common for other regions. Carbonate and quartz minerals are modeled below 10% for all low-dust regions.
2. Ten mineral assemblage classes are statistically separable at ~300 km spatial scales in Martian low-dust regions (Figure 5c and Table 4). Boundaries in mineral assemblage observed by *Christensen et al*. [2000], *Hoefen et al*. [2003], *Hamilton and Christensen* [2005], *Rogers et al*. [2007], *Rogers and Christensen* [2007], and *Koeppen and Hamilton* [2008] (Syrtis Major, Thaumasia Planum, Acidalia, Meridiani hematite unit, and Nili Fossae olivine-bearing unit) are preserved in the new class maps; and new distinctions are apparent.
3. Sinus Meridiani, the low-dust region bordering the southern margin of the Meridiani Planum hematite unit, is compositionally distinct from similarly aged heavily cratered terrains. Its class is characterized by lower feldspar, and higher-sulfate and high-Si phase abundance than other low-dust surfaces on Mars. Class 6 exhibits a distinctly higher H_2O abundance mode in GRS data (Figures 8, 9, and S1), and a moderately higher Fe abundance, compared to other low-dust regions. Together, the Fe, H_2O and TES sulfate abundances may point to a higher proportion of iron sulfates in the Sinus Meridiani soils. Additionally, the region shares some common compositional traits with Meridiani Planum, namely, a lower feldspar abundance and slightly higher sulfate and high-silica phase abundance. Thus, it is possible that Sinus Meridiani may share at least part of common history with Meridiani Planum (section 5.2).
4. Hesperian volcanic provinces in the highlands (Hesperia Planum, Thaumasia, Protei Regio, and portions of Syrtis Major) largely fall into the same TES compositional class (Class 8), which is characterized by elevated HCP abundance compared to most other highlands classes. This is consistent with previous studies showing a decrease in LCP/(LCP + HCP) from Noachian to Hesperian terrains [e.g., *Mustard et al*., 2005; *Poulet et al*., 2009]; our work demonstrates that this trend is present on a larger scale. We show that these Hesperian highland volcanic provinces are chemically distinct from the cratered terrain Classes (4–6), with all exhibiting relatively low K concentrations and low-to-intermediate Th concentrations. This trend could be due to depletion of incompatible elements from mantle source materials after formation of the Noachian crust, or to magmatic differentiation processes during the Noachian to increase K and Th.
5. Syrtis Major may be split into two classes. Areas in north central and south central Syrtis Major (Class 3) exhibit higher abundances of HCP relative to areas around the periphery and in the west central portions of the shield (Class 8). This new distinction made in the thermal infrared corresponds remarkably well with spectral distinctions made in a recent Syrtis mapping effort by [*Clenet et al*., 2013] using OMEGA VNIR data. Our work shows that CRISM HCP parameter distributions are also distinct between the two classes at the $>$99% confidence level.
6. Northern and southern Acidalia are compositionally distinct. Though this distinction has been noted before by *Farrand et al*. [2000], *Dobrea et al*. [2003], and *Rogers et al*. [2007], it is so compelling that it bears repeating. The mineralogic boundary generally coincides with a geomorphologic boundary

between hummocky terrain and subdued hummocky terrain with polygonally patterned ground, which may indicate that the compositional differences relate to the extent of periglacial activity and aqueous weathering in ice-rich soils in the north [*Kraft et al*., 2010].

7. Nearly all of the compositional boundaries apparent in the TES-derived class map are discernible in GRS elemental mass fraction data. This correspondence provides an indication of the minimum depth that these classes represent and suggests that igneous processes and large-scale sedimentary and/or glacial processes (e.g., Hellas basin fill, southern Acidalia outwash, northern Acidalia periglacial activity) are the primary control on spatial variations in composition. Though some of the mineralogical characteristics are likely reflective of surficial weathering processes (e.g., oxidative weathering or alteration by thin transient films of water), any secondary mineral assemblages that are present as thin coatings must be controlled by the underlying primary mineralogy.
8. Terrains that are distinct based on geomorphology and age tend to also exhibit distinct compositions, which is inconsistent with the previous suggestion of a globally homogeneous basaltic soil.

Acknowledgments

We thank Suniti Karunatillake and Olivier Gasnault for useful discussions regarding some of the methodologies used in this work. We appreciate the reviews from Violaine Sautter, David Baratoux, Jeff Taylor and one anonymous person, all whom contributed useful comments and suggestions that improved the original manuscript. We thank Anouck Ody for providing a null data mask for the OMEGA spectral parameter maps used here. The incorporation of global maps of CRISM multispectral summary parameters would not have been possible without the efforts of Dale Noss. This work was funded by the NASA Mars Data Analysis program, under grant NNX09AI47G (VEH). All data used in this work are available from the NASA Planetary Data System (http://pds.nasa.gov).

References

Andrews-Hanna, J. C., M. T. Zuber, R. E. Arvidson, and S. M. Wiseman (2010), Early Mars hydrology: Meridiani playa deposits and the sedimentary record of Arabia Terra, *J. Geophys. Res.*, *115*, E06002, doi:10.1029/2009JE003485.

Ansan, V., et al. (2011), Stratigraphy, mineralogy, and origin of layered deposits inside Terby crater, Mars, *Icarus*, *211*(1), 273–304, doi:10.1016/j.icarus.2010.09.011.

Bandfield, J. L. (2002), Global mineral distributions on Mars, *J. Geophys. Res.*, *107*(E6), 5042, doi:10.1029/2001JE001510.

Bandfield, J. L. (2006), Extended surface exposures of granitoid compositions in Syrtis Major, Mars, *Geophys. Res. Lett.*, *33*, L06203, doi:10.1029/2005GL025559.

Bandfield, J. L. (2008), High-silica deposits of an aqueous origin in western Hellas Basin, Mars, *Geophys. Res. Lett.*, *35*, L12205, doi:10.1029/2008GL033807.

Bandfield, J. L., and A. D. Rogers (2008), Olivine dissolution by acidic fluids in Argyre Planitia, Mars: Evidence for a widespread process?, *Geology*, *36*(7), 579–582.

Bandfield, J. L., V. E. Hamilton, and P. R. Christensen (2000a), A global view of Martian surface compositions from MGS-TES, *Science*, *287*(5458), 1626–1630.

Bandfield, J. L., P. R. Christensen, and M. D. Smith (2000b), Spectral data set factor analysis and end-member recovery: Application to analysis of Martian atmospheric particulates, *J. Geophys. Res.*, *105*, 9573–9587, doi:10.1029/1999JE001094.

Bandfield, J. L., A. D. Rogers, and C. S. Edwards (2011), The role of aqueous alteration in the formation of Martian soils, *Icarus*, *211*(1), 157–171, doi:10.1016/j.icarus.2010.08.028.

Baratoux, D., P. Pinet, A. Gendrin, L. Kanner, J. Mustard, Y. Daydou, J. Vaucher, and J.-P. Bibring (2007), Mineralogical structure of the subsurface of Syrtis Major from OMEGA observations of lobate ejecta blankets, *J. Geophys. Res.*, *112*, E08S05, doi:10.1029/2007JE002890.

Baratoux, D., M. J. Toplis, M. Monnereau, and O. Gasnault (2011), Thermal history of Mars inferred from orbital geochemistry of volcanic provinces, *Nature*, *472*(7343), 338–341, doi:10.1038/nature09903.

Baratoux, D., M. J. Toplis, M. Monnereau, and V. Sautter (2013), The petrological expression of early Mars volcanism, *J. Geophys. Res. Planets*, *118*, 59–64, doi:10.1029/2012JE004234.

Bell, J. F., III (2008), *The Martian Surface: Composition, Mineralogy, and Physical Properties*, Cambridge Univ. Press, New York.

Bish, D. L., et al. (2013), X-ray diffraction results from Mars Science Laboratory: Mineralogy of Rocknest at Gale crater, *Science*, *341*(6153), 1238932, doi:10.1126/science.1238932.

Boynton, W. V., et al. (2004), The Mars odyssey gamma-ray spectrometer instrument suite, *Space Sci. Rev.*, *110*, 37–83.

Boynton, W. V., et al. (2007), Concentration of H, Si, Cl, K, Fe, and Th in the low- and mid-latitude regions of Mars, *J. Geophys. Res.*, *112*, E12S99, doi:10.1029/2007JE002887.

Burt, J. E., G. M. Barber, and D. L. Rigby (2009), *Elementary Statistics for Geographers*, The Guilford Press, New York.

Carr, M. H. (1995), The Martian drainage system and the origin of valley networks and fretted channels, *J. Geophys. Res.*, *100*, 7479–7507, doi:10.1029/95JE00260.

Carter, J., F. Poulet, J.-P. Bibring, N. Mangold, and S. Murchie (2013), Hydrous minerals on Mars as seen by the CRISM and OMEGA imaging spectrometers: Updated global view, *J. Geophys. Res. Planets*, *118*, 831–858, doi:10.1029/2012JE004145.

Christensen, P. R., and H. J. Moore (1992), The Martian surface layer, in *Mars*, edited by H. H. Kieffer et al., pp. 686–729, Univ. of Ariz. Press, Tuscon, Ariz.

Christensen, P. R., et al. (2000), Detection of crystalline hematite mineralization on Mars by the Thermal Emission Spectrometer: Evidence for near-surface water, *J. Geophys. Res.*, *105*, 9623–9642, doi:10.1029/1999JE001093.

Christensen, P. R., et al. (2001), Mars Global Surveyor Thermal Emission Spectrometer experiment: Investigation description and surface science results, *J. Geophys. Res.*, *106*, 23,823–23,871, doi:10.1029/2000JE001370.

Clark, R. N., and T. L. Roush (1984), Reflectance spectroscopy: Quantitative analysis techniques for remote sensing applications, *J. Geophys. Res.*, *89*, 6329–6340, doi:10.1029/JB089iB07p06329.

Clenet, H., P. Pinet, G. Ceuleneer, Y. Daydou, F. Heuripeau, C. Rosemberg, J.-P. Bibring, G. Bellucci, F. Altieri, and B. Gondet (2013), A systematic mapping procedure based on the Modified Gaussian Model to characterize magmatic units from olivine/pyroxenes mixtures: Application to the Syrtis Major volcanic shield on Mars, *J. Geophys. Res. Planets*, *118*, 1632–1655, doi:10.1002/jgre.20112.

Cloutis, E. A., M. A. Craig, R. V. Kruzelecky, W. R. Jamroz, A. Scott, F. C. Hawthorne, and S. A. Mertzman (2008), Spectral reflectance properties of minerals exposed to simulated Mars surface conditions, *Icarus*, *195*(1), 140–168, doi:10.1016/j.icarus.2007.10.028.

Cousin, A., et al. (2014), Compositions of coarse and fine particles in martian soils at gale: A window into the production of soils, *Icarus*, doi:10.1016/j.icarus.2014.04.052, in press.

Craddock, R. A., and A. D. Howard (2002), The case for rainfall on a warm, wet early Mars, *J. Geophys. Res.*, *107*(E11), 5111, doi:10.1029/2001JE001505.

Crown, D. A., L. F. Bleamaster, and S. C. Mest (2005), Styles and timing of volatile-driven activity in the eastern Hellas region of Mars, *J. Geophys. Res.*, *110*, E12S22, doi:10.1029/2005JE002496.
Crown, D. A., L. F. Bleamaster, S. C. Mest, J. F. Mustard, and M. Vincendon (2010), Geologic Mapping of the NW Rim Of Hellas Basin, Mars: Evidence for an ancient buried landscape, 41st Lunar Planet Sci. Abs. 1888.
Dobrea, E. Z. N., J. F. Bell, M. J. Wolff, and K. D. Gordon (2003), H2O- and OH-bearing minerals in the Martian regolith: Analysis of 1997 observations from HST/NICMOS, *Icarus*, *166*(1), 1–20.
Ehlmann, B. L., and J. F. Mustard (2012), An in-situ record of major environmental transitions on early Mars at Northeast Syrtis Major, *Geophys. Res. Lett.*, *39*, L11202, doi:10.1029/2012GL051594.
Farrand, W. H., J. F. Bell III, R. V. Morris, and M. J. Wolff (2000), Global color units on Mars from 199 9 HST/WFPC2 imaging data, *Bull. Am. Astron. Soc.*, *32*, Abstract 1119.
Fassett, C. I., and J. W. Head (2008), The timing of Martian valley network activity: Constraints from buffered crater counting, *Icarus*, *195*(1), 61–89, doi:10.1016/j.icarus.2007.12.009.
Feldman, W. C., et al. (2002), Global distribution of neutrons from Mars: Results from Mars Odyssey, *Science*, *297*(5578), 75–78.
Filiberto, J., and A. H. Treiman (2009), The effect of chlorine on the liquidus of basalt: First results and implications for basalt genesis on Mars and Earth, *Chem. Geol.*, *263*, 60–68, doi:10.1016/j.chemgeo.2008.08.025.
Gaffey, S. J., L. A. McFadden, D. B. Nash, and C. M. Pieters (1993), Ultraviolet, visible, and near-infrared reflectance spectroscopy: Laboratory spectra of geological materials, in *Remote Geochemical Analysis: Elemental and Mineralogical Composition*, edited by C. M. Pieters and P. A. J. Englert, pp. 43–77, Cambridge Univ. Press, Cambridge, U. K.
Gasnault, O., G. J. Taylor, S. Karunatillake, J. Dohm, H. Newsom, O. Forni, P. Pinet, and W. V. Boynton (2010), Quantitative geochemical mapping of Martian elemental provinces, *Icarus*, *207*(1), 226–247, doi:10.1016/j.icarus.2009.11.010.
Golombek, M. P., et al. (2003), Selection of the Mars Exploration Rover landing sites, *J. Geophys. Res.*, *108*(E12), 8072, doi:10.1029/2003JE002074.
Greeley, R., and J. E. Guest (1987), Geologic map of the eastern equatorial region of Mars.
Hahn, B. C., et al. (2007), Mars Odyssey Gamma Ray Spectrometer elemental abundances and apparent relative surface age: Implications for Martian crustal evolution, *J. Geophys. Res.*, *112*, E03S11, doi:10.1029/2006JE002821.
Hamilton, V. E. (2000), Thermal infrared spectroscopy of the pyroxene mineral series, *J. Geophys. Res.*, *105*, 9701–9716, doi:10.1029/1999JE001112.
Hamilton, V. E., and P. R. Christensen (2005), Evidence for extensive, olivine-rich bedrock on Mars, *Geology*, *33*(6), 433–436.
Hamilton, V. E., P. R. Christensen, and H. Y. McSween Jr. (1997), Determination of Martian meteorite lithologies and mineralogies using vibrational spectroscopy, *J. Geophys. Res.*, *102*, 25,593–25,603, doi:10.1029/97JE01874.
Hamilton, V. E., P. R. Christensen, H. Y. McSween, and J. L. Bandfield (2003), Searching for the source regions of Martian meteorites using MGS TES: Integrating Martian meteorites into the global distribution of igneous materials on Mars, *Meteorit. Planet. Sci.*, *38*(6), 871–885.
Hoefen, T. M., R. N. Clark, J. L. Bandfield, M. D. Smith, J. C. Pearl, and P. R. Christensen (2003), Discovery of olivine in the Nili Fossae region of Mars, *Science*, *302*(5645), 627–630.
Horgan, B. H. N., E. A. Cloutis, P. Mann, and J. F. Bell (2014), Near-infrared spectra of ferrous mineral mixtures and methods for their identification in planetary surface spectra, *Icarus*, *234*, 132–154, doi:10.1016/j.icarus.2014.02.031.
Hynek, B. M., M. Beach, and M. R. T. Hoke (2010), Updated global map of Martian valley networks and implications for climate and hydrologic processes, *J. Geophys. Res.*, *115*, E09008, doi:10.1029/2009JE003548.
Hyvärinen, A., and E. Oja (2000), Independent component analysis: Algorithms and applications, *Neural Networks*, *13*(4–5), 411–430.
Jodlowski, P., T. Platz, and G. G. Michael (2013), Eruption history of the Syrtis Major Volcanic Province, Mars, 44th Lunar Planet. Sci. Conf., Abstract #2322.
Karunatillake, S., et al. (2006), Composition of northern low-albedo regions of Mars: Insights from the Mars Odyssey Gamma Ray Spectrometer, *J. Geophys. Res.*, *111*, E03S05, doi:10.1029/2006JE002675.
Karunatillake, S., J. J. Wray, S. W. Squyres, G. J. Taylor, O. Gasnault, S. M. McLennan, W. Boynton, M. R. El Maarry, and J. M. Dohm (2009), Chemically striking regions on Mars and Stealth revisited, *J. Geophys. Res.*, *114*, E12001, doi:10.1029/2008JE003303.
Koeppen, W. C., and V. E. Hamilton (2008), Global distribution, composition, and abundance of olivine on the surface of Mars from thermal infrared data, *J. Geophys. Res.*, *113*, E05001, doi:10.1029/2007JE002984.
Korteniemi, J., V.-P. Kostama, T. Törmänen, M. Aittola, T. Öhman, H. Lahtela, J. Raitala, and G. Neukum (2005), Complex geology of two large impact craters in Tyrrhena Terra, Mars: Detailed analysis using MEX HRSC camera data, *J. Geophys. Res.*, *110*, E12S18, doi:10.1029/2005JE002427.
Kraft, M. D., J. R. Michalski, and T. G. Sharp (2003), Effects of pure silica coatings on thermal emission spectra of basaltic rocks: Considerations for Martian surface mineralogy, *Geophys. Res. Lett.*, *30*(24), 2288, doi:10.1029/2003GL018848.
Kraft, M. D., A. D. Rogers, R. L. Fergason, J. R. Michalski, and T. G. Sharp (2010), Spectral and geomorphic evidence for chemical weathering in the icy plains of Acidalia Planitia, Mars, 41st Lunar and Planetary Science Conference, Abstract #2600. [Available at http://www.lpi.usra.edu/meetings/lpsc2010/pdf/2600.pdf.]
Kruse, F. A., A. B. Lefkoff, J. B. Boardman, K. B. Heidebrecht, A. T. Shapiro, P. J. Barloon, and A. F. H. Goetz (1993), The Spectral Image Processing System (SIPS)—Interactive visualization and analysis of imaging spectrometer data, *Remote Sens. Environ.*, *44*, 145–163.
Leonard, G. J., and K. L. Tanaka (2001), Geologic map of the Hellas Region of Mars, scale 1:5000,000, USGS Geologic Investigations Series I-2694.
Malin, M. C., and K. S. Edgett (2000), Sedimentary rocks of early Mars, *Science*, *290*(5498), 1927–1937.
McLennan, S. M. (2003), Sedimentary silica on Mars, *Geology*, *31*(4), 315–318.
Meslin, P.-Y., et al. (2013), Soil diversity and hydration as observed by ChemCam at Gale crater, Mars, *Science*, *341*(6153), 1238670, doi:10.1126/science.1238670.
Mest, S. C., and D. A. Crown (2005), Millochau crater, Mars: Infilling and erosion of an ancient highland impact crater, *Icarus*, *175*(2), 335–359, doi:10.1016/j.icarus.2004.12.008.
Michalski, J. R., M. D. Kraft, T. G. Sharp, L. B. Williams, and P. R. Christensen (2005), Mineralogical constraints on the high-silica Martian surface component observed by TES, *Icarus*, *174*(1), 161–177.
Michalski, J. R., M. D. Kraft, T. G. Sharp, L. B. Williams, and P. R. Christensen (2006), Emission spectroscopy of clay minerals and evidence for poorly crystalline aluminosilicates on Mars from Thermal Emission Spectrometer data, *J. Geophys. Res.*, *111*, E03004, doi:10.1029/2005JE002438.
Milliken, R. E., and J. F. Mustard (2005), Quantifying absolute water content of minerals using near-infrared reflectance spectroscopy, *J. Geophys. Res.*, *110*, E12001, doi:10.1029/2005JE002534.
Minitti, M. E., C. M. Weitz, M. D. Lane, and J. L. Bishop (2007), Morphology, chemistry, and spectral properties of Hawaiian rock coatings and implications for Mars, *J. Geophys. Res.*, *112*, E05015, doi:10.1029/2006JE002839.

Moore, J. M., and A. D. Howard (2005), Large alluvial fans on Mars, *J. Geophys. Res.*, *110*, E04005, doi:10.1029/2004JE002352.
Moore, J. M., and D. E. Wilhelms (2001), Hellas as a possible site of ancient ice-covered lakes on Mars, *Icarus*, *154*, 258–276.
Murchie, S., et al. (2007), Compact reconnaissance Imaging Spectrometer for Mars (CRISM) on Mars Reconnaissance Orbiter (MRO), *J. Geophys. Res.*, *112*, E05S03, doi:10.1029/2006JE002682.
Mustard, J. F., F. Poulet, A. Gendrin, J.-P. P. Bibring, Y. Langevin, B. Gondet, N. Mangold, G. Bellucci, and F. Altieri (2005), Olivine and pyroxene diversity in the crust of Mars, *Science*, *307*(5715), 1594–1597, doi:10.1126/science.1109098.
Mustard, J. F., F. Poulet, J. W. Head, N. Mangold, J. P. Bibring, S. M. Pelkey, C. I. Fasset, Y. Langevin, and G. Neukum (2007), Mineralogy of the Nili Fossae region with OMEGA/Mex data: 1. Ancient impact melt in the Isidis Basin and implications for the transition from the Noachian to Hesperian, *J. Geophys. Res.*, *112*, E08S03, doi:10.1029/2006JE002834.
Ody, A., F. Poulet, Y. Langevin, J.-P. Bibring, G. Bellucci, F. Altieri, B. Gondet, M. Vincendon, J. Carter, and N. Manaud (2012), Global maps of anhydrous minerals at the surface of Mars from OMEGA/MEx, *J. Geophys. Res.*, *117*, E00J14, doi:10.1029/2012JE004117.
Ody, A., F. Poulet, J.-P. Bibring, D. Loizeau, J. Carter, B. Gondet, and Y. Langevin (2013), Global investigation of olivine on Mars: Insights into crust and mantle compositions, *J. Geophys. Res. Planets*, *118*, 234–262, doi:10.1029/2012JE004149.
Pelkey, S. M., et al. (2007), CRISM multispectral summary products: Parameterizing mineral diversity on Mars from reflectance, *J. Geophys. Res.*, *112*, E08S14, doi:10.1029/2006JE002831.
Poulet, F., C. Gomez, J.-P. Bibring, Y. Langevin, B. Gondet, P. Pinet, G. Belluci, and J. Mustard (2007), Martian surface mineralogy from Observatoire pour la Minéralogie, l'Eau, les Glaces et l'Activité on board the Mars Express spacecraft (OMEGA/MEx): Global mineral maps, *J. Geophys. Res.*, *112*, E08S02, doi:10.1029/2006JE002840.
Poulet, F., J. P. Bibring, Y. Langevin, J. F. Mustard, N. Mangold, M. Vincendon, B. Gondet, P. Pinet, J. M. Bardintzeff, and B. Platevoet (2009), Quantitative compositional analysis of Martian mafic regions using the MEx/OMEGA reflectance data, *Icarus*, *201*(1), 69–83.
Ramsey, M. S., and P. R. Christensen (1998), Quantitative deconvolution of thermal emission spectra, *J. Geophys. Res.*, *103*, 577–596, doi:10.1029/97JB02784.
Richards, J. A., and X. Jia (2006), *Remote Sensing Digital Image Analysis: An Introduction*, pp. 232–234, Springer, Heidelberg, Germany.
Rogers, A. D., and O. Aharonson (2008), Mineralogical composition of sands in Meridiani Planum determined from MER data and comparison to orbital measurements, *J. Geophys. Res.*, *113*, E06S14, doi:10.1029/2007JE002995.
Rogers, A. D., and P. R. Christensen (2007), Surface mineralogy of Martian low-albedo regions from MGS-TES data: Implications for upper crustal evolution and surface alteration, *J. Geophys. Res.*, *112*, E01003, doi:10.1029/2006JE002727.
Rogers, A. D., and R. L. Fergason (2011), Regional-scale stratigraphy of surface units in Tyrrhena and Iapygia Terrae, Mars: Insights into highland crustal evolution and alteration history, *J. Geophys. Res.*, *116*, E08005, doi:10.1029/2010JE003772.
Rogers, A. D., J. L. Bandfield, and P. R. Christensen (2007), Global spectral classification of Martian low-albedo regions with Mars Global Surveyor Thermal Emission Spectrometer (MGS-TES) data, *J. Geophys. Res.*, *112*, E02004, doi:10.1029/2006JE002726.
Ruff, S. W., and P. R. Christensen (2007), Basaltic andesite, altered basalt, and a TES-based search for smectite clay minerals on Mars, *Geophys. Res. Lett.*, *34*, L10204, doi:10.1029/2007GL029602.
Salvatore, M. R., J. F. Mustard, J. W. Head, R. F. Cooper, D. R. Marchant, and M. B. Wyatt (2013), Development of alteration rinds by oxidative weathering processes in Beacon Valley, Antarctica, and implications for Mars, *Geochim. Cosmochim. Acta*, *115*, 137–161, doi:10.1016/j.gca.2013.04.002.
Scott, D. H., and K. L. Tanaka (1986), Geologic map of the western equatorial region of Mars, 1:15,000,000.
Seelos, F. P., S. L. Murchie, D. C. Humm, O. S. Barnouin, F. Morgan, H. W. Taylor, C. Hash, and the CRISM Team (2011), CRISM data processing and analysis products update—Calibration, correction, and visualization, LPSC 42, Abstract #1438.
Segura, T. L., O. B. Toon, A. Colaprete, and K. Zahnle (2002), Environmental effects of large impacts on Mars, *Science*, *298*, 1977–1980, doi:10.1126/science.1073586.
Smith, M. D., J. L. Bandfield, and P. R. Christensen (2000), Separation of atmospheric and surface spectral features in Mars Global Surveyor Thermal Emission Spectrometer (TES) spectra, *J. Geophys. Res.*, *105*, 9589–9607, doi:10.1029/1999JE001105.
Stepinski, T. F., and A. P. Stepinski (2005), Morphology of drainage basins as an indicator of climate on early Mars, *J. Geophys. Res.*, *110*, E12S12, doi:10.1029/2005JE002448.
Swain, P. H., and S. M. Davis (1978), *Remote Sensing: The Quantitative Approach*, pp. 1–396, McGraw-Hill, New York.
Tanaka, K. L., and G. J. Leonard (1995), Geology and landscape evolution of the Hellas region of Mars, *J. Geophys. Res.*, *100*, 5407–5432, doi:10.1029/94JE02804.
Tanaka, K. L., and D. H. Scott (1987), Geologic map of the polar regions of Mars, scale 1:15,000,000.
Taylor, G. J., et al. (2006), Variations in K/Th on Mars, *J. Geophys. Res.*, *111*, E03S06, doi:10.1029/2006JE002676.
Taylor, G. J., L. M. V. Martel, S. Karunatillake, O. Gasnault, and W. V. Boynton (2010), Mapping Mars geochemically, *Geology*, *38*(2), 183–186, doi:10.1130/g30470.1.
Tosca, N. J., S. M. McLennan, D. H. Lindsley, and M. A. A. Schoonen (2004), Acid-sulfate weathering of synthetic Martian basalt: The acid fog model revisited, *J. Geophys. Res.*, *109*, E05003, doi:10.1029/2003JE002218.
Ustunisik, G., H. Nekvasil, F. M. McCubbin, and D. H. Lindsley (2010), The effect of S and Cl on mineral stability in Martian Magmas, *41st Lunar Planet. Sci. Conf.*, Abstract #1761.
Wichman, R. W., and P. H. Schultz (1989), Sequence and mechanisms of deformation around the Hellas and Isidis impact basins on Mars, *J. Geophys. Res.*, *94*, 17,333–17,357, doi:10.1029/JB094iB12p17333.
Wilson, S. A., A. D. Howard, J. M. Moore, and J. A. Grant (2007), Geomorphic and stratigraphic analysis of Crater Terby and layered deposits north of Hellas basin, Mars, *J. Geophys. Res.*, *112*, E08009, doi:10.1029/2006JE002830.
Wyatt, M. B., and H. Y. McSween (2002), Spectral evidence for weathered basalt as an alternative to andesite in the northern lowlands of Mars, *Nature*, *417*(6886), 263–266.
Wyatt, M. B., H. Y. McSween, K. L. Tanaka, and J. W. Head (2004), Global geologic context for rock types and surface alteration on Mars, *Geology*, *32*(8), 645–648.
Yen, A. S., et al. (2005), An integrated view of the chemistry and mineralogy of martian soils, *Nature*, *436*(7047), 49–54.